Article

Developmental Cell

Directed cell invasion and asymmetric adhesion drive tissue elongation and turning in *C. elegans* gonad morphogenesis

Graphical abstract

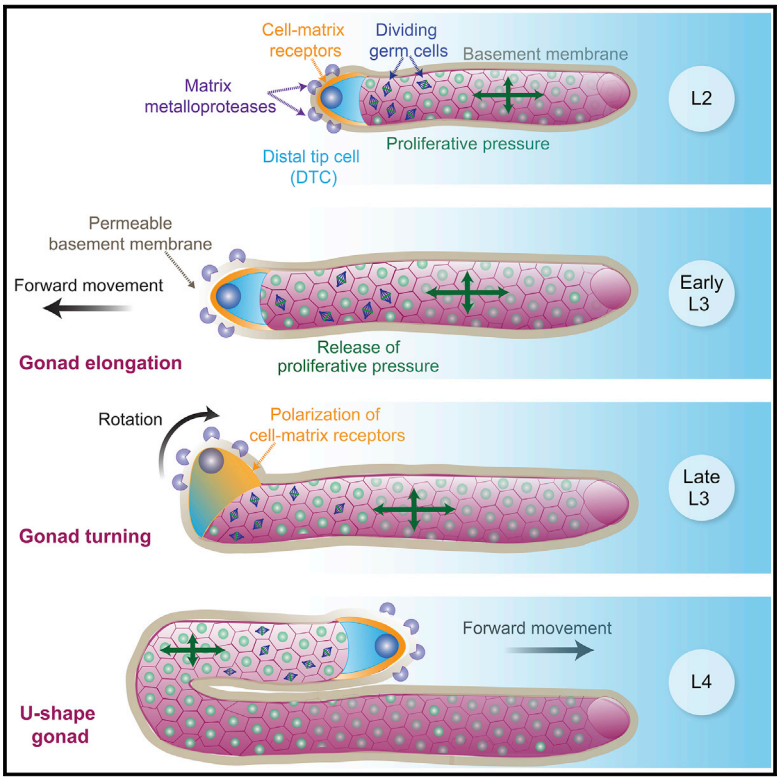

Highlights

- Distal tip cell (DTC) in *C. elegans* hermaphrodite gonad is pushed by proliferating germ cells
- Extracellular matrix (ECM) degradation by the DTC directs gonad elongation
- DTC-ECM adhesion polarity drives gonadal turning
- CDC-42 and SRC regulate DTC integrin polarity during the turn

Authors

Priti Agarwal, Tom Shemesh, Ronen Zaidel-Bar

Correspondence

tomsh@technion.ac.il (T.S.), zaidelbar@tauex.tau.ac.il (R.Z.-B.)

In brief

Agarwal et al. investigate the mechanics of *C. elegans* gonad morphogenesis in this study. They show that tissue elongation results from leader cell invasion powered by localized matrix degradation and the proliferative pressure of follower cells, while asymmetric cell-ECM adhesion creates torque that drives the U-turning of the gonad.

Agarwal et al., 2022, Developmental Cell *57*, 1–16
September 12, 2022
https://doi.org/10.1016/j.devcel.2022.08.003

CellPress

Please cite this article in press as: Agarwal et al., Directed cell invasion and asymmetric adhesion drive tissue elongation and turning in *C. elegans* gonad morphogenesis, Developmental Cell (2022), https://doi.org/10.1016/j.devcel.2022.08.003

Developmental Cell

CellPress

Article

Directed cell invasion and asymmetric adhesion drive tissue elongation and turning in *C. elegans* gonad morphogenesis

Priti Agarwal,[1] Tom Shemesh,[2,*] and Ronen Zaidel-Bar[1,3,*]
[1]Department of Cell and Developmental Biology, Faculty of Medicine, Tel Aviv University, Tel Aviv 6997801, Israel
[2]Faculty of Biology, Technion—Israel Institute of Technology, Haifa 3200003, Israel
[3]Lead contact
*Correspondence: tomsh@technion.ac.il (T.S.), zaidelbar@tauex.tau.ac.il (R.Z.-B.)
https://doi.org/10.1016/j.devcel.2022.08.003

SUMMARY

Development of the *C. elegans* gonad has long been studied as a model of organogenesis driven by collective cell migration. A somatic cell named the distal tip cell (DTC) is thought to serve as the leader of following germ cells; yet, the mechanism for DTC propulsion and maneuvering remains elusive. Here, we demonstrate that the DTC is not self-propelled but rather is pushed by the proliferating germ cells. Proliferative pressure pushes the DTC forward, against the resistance of the basement membrane in front. The DTC locally secretes metalloproteases that degrade the impeding membrane, resulting in gonad elongation. Turning of the gonad is achieved by polarized DTC-matrix adhesions. The asymmetrical traction results in a bending moment on the DTC. Src and Cdc42 regulate integrin adhesion polarity, whereas an external netrin signal determines DTC orientation. Our findings challenge the current view of DTC migration and offer a distinct framework to understand organogenesis.

INTRODUCTION

Every organ has a specialized architecture that is critical for its function. Organ formation involves multiple developmental processes, including cell fate determination, proliferation, and cell migration, which are regulated by biochemical signals as well as mechanical forces (Agarwal and Zaidel-Bar, 2021; Gilmour et al., 2017; Petridou et al., 2017). Several strategies for organ elongation have been described, including cell migration, cell intercalation, cell shape change, oriented cell division (Andrew and Ewald, 2010), as well as tissue mechanics (Mongera et al., 2018). Yet, the cellular mechanisms that guide tissue elongation and folding to arrive at the desired 3D organ shape are still poorly understood. Here, we address this question by studying the morphogenesis of the nematode *Caenorhabditis elegans* gonad.

The two-armed symmetrical gonad of the hermaphrodite *C. elegans* begins to develop post embryonically. Germ cells are surrounded by somatic sheath cells and a basement membrane (Hall et al., 1999; Huang et al., 2003; Killian and Hubbard, 2005), and are capped at the ends of the arms by two somatic distal tip cells (DTCs). The DTCs function as germline stem cell niches, supporting proliferation (Kershner et al., 2014; Kimble, 2005). Starting at the second larval stage (L2), the two gonadal arms grow and elongate in opposite directions along the ventral side, and at the onset of the third larval stage (L3), both gonad arms perform U-shaped turns and continue to elongate toward each other along the dorsal side in the fourth larval stage (L4). At the onset of young adulthood, when each gonad arm reaches a length of ~370 μm, the elongation stops, ~45 h after it began, and the gonad assumes its reproductive function (Hedgecock et al., 1987; Nishiwaki, 1999) (Figure 1A). Current models assume that gonad development is predominantly driven by active DTC migration (Cecchetelli and Cram, 2017; Sherwood and Plastino, 2018; Wong and Schwarzbauer, 2012). This view is based on the position of the DTC at the front of the elongating gonad, on the gonad morphogenesis defects observed when known migration and chemotactic proteins (e.g., integrins and netrin) are depleted, and on the finding that the male linker cell (considered the male counterpart of the hermaphrodite DTC) can migrate independently of the gonad. However, DTC morphology is strikingly different from that of the linker cell and no direct evidence for independent DTC propulsion exists. Therefore, the mechanism of gonad elongation and folding remains unresolved.

In this paper, we reveal the cellular basis for morphogenesis of the *C. elegans* hermaphrodite gonad: it depends on the combined contributions of proliferating germ cells, which provide a pushing force, and the somatic DTC, which acts as the pilot by secreting metalloproteases and selectively engaging cell-matrix adhesions.

RESULTS

DTC is polarized but lacks any protrusive structures at the front

Cell migration is typically characterized by F-actin-rich structures, including lamellipodia, filopodia, blebs, or lobopodia

Please cite this article in press as: Agarwal et al., Directed cell invasion and asymmetric adhesion drive tissue elongation and turning in *C. elegans* gonad morphogenesis, Developmental Cell (2022), https://doi.org/10.1016/j.devcel.2022.08.003

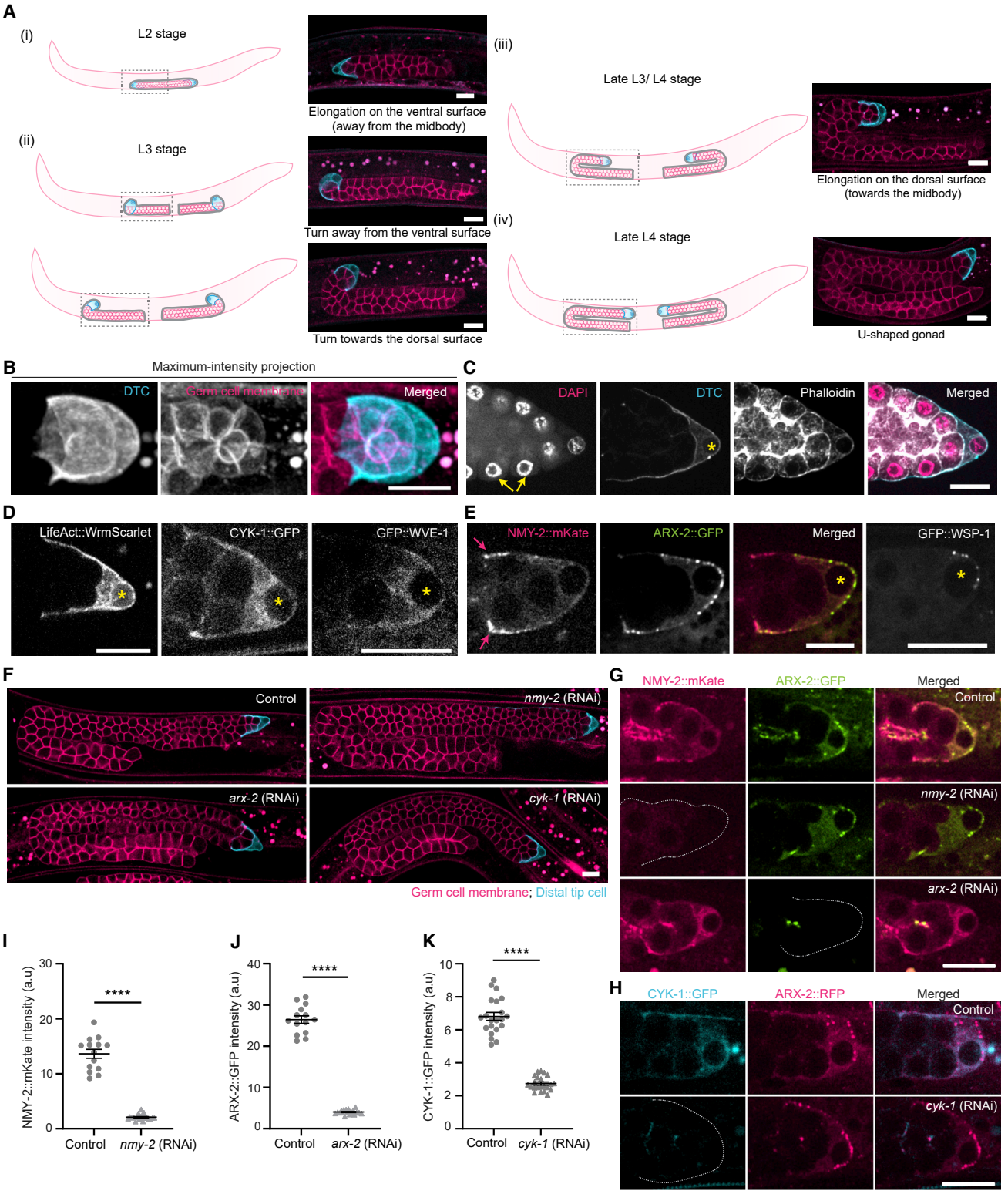

Figure 1. DTC migration does not involve actin protrusions or actomyosin contractility

(A) Schematic illustration of the progression of gonad development from larval stage 2 (L2) until late larval stage 4 (L4) with corresponding microscopic images. Each gonadal arm, surrounded by basement membrane (gray), houses germ cells (pink), and a single distal tip cell (DTC) (cyan) caps its end. The microscopic images depict one gonad arm expressing *lag-2p*::mNG::PH (cyan), as a DTC membrane marker, and *pie-1p::mCherry::PH(PLC1delta1)* (pink), as a germ cell membrane marker.

(legend continued on next page)

Please cite this article in press as: Agarwal et al., Directed cell invasion and asymmetric adhesion drive tissue elongation and turning in *C. elegans* gonad morphogenesis, Developmental Cell (2022), https://doi.org/10.1016/j.devcel.2022.08.003

(Agarwal and Zaidel-Bar, 2019). However, close examination of a fluorescent membrane marker and 3D reconstructed images of the DTC revealed that DTCs lack any protrusions at their leading edge (Figures 1B and S1). Consistently, phalloidin staining of fixed gonads and LifeAct::wrmScarlet expression in DTCs of L4-stage worms both showed F-actin enrichment at the cortical and perinuclear region of the DTC but did not show any actin-rich protrusions at the front (Figures 1C and 1D). Also, the endogenously tagged actin regulators, formin (CYK-1) and WAVE/SCAR (WVE-1), were found homogenously within the DTC and did not reveal any protrusions (Figure 1D).

Another characteristic of migratory cells is the establishment of front-to-rear cytoskeletal polarity (Etienne-Manneville, 2008; Rappel and Edelstein-Keshet, 2017; Ridley et al., 2003). To test whether DTCs are polarized, we examined multiple endogenously tagged cytoskeletal proteins. Non-muscle myosin-II (NMY-2) showed enrichment at the rear end of DTCs, behind the nucleus, while the actin nucleator Arp2/3 complex (ARX-2) and its activator WASP protein (WSP-1) formed clusters at the front (Figure 1E). Thus, actin and myosin are polarized in the DTC, but it lacks protrusions at the leading edge.

DTC movement is independent of myosin-II contractility and actin polymerization

The absence of any protrusive structures suggested that the DTC may not necessarily be driven by active migration. A prerequisite for autonomous cell motility is mechanical force generation by actin polymerization and/or the contractile actomyosin machinery (Agarwal and Zaidel-Bar, 2019; Blanchoin et al., 2014). Therefore, we examined the requirement of NMY-2, ARX-2, or CYK-1 for DTC motility by depleting them specifically in the DTC, employing a DTC-specific RNAi strain that is also hypersensitive to RNAi (Linden et al., 2017). DTC-specific RNAi of *nmy-2* (n = 65), *arx-2* (n = 55), or *cyk-1* (n = 70) did not affect DTC migration and the gonad elongated normally, forming the stereotypical U-shaped architecture as observed in control worms (n = 86) (Figure 1F). We confirmed the efficacy of knockdown by depleting *nmy-2, arx-2*, or *cyk-1* in the background of endogenously fluorescently tagged proteins. *nmy-2* (RNAi), *arx-2* (RNAi), and *cyk-1* (RNAi) reduced the fluorescence intensity of NMY-2::mKate, ARX-2::GFP, and CYK-1::GFP to 14%, 15%, and 40%, respectively, as compared with the control (Figures 1G–1K). These findings suggested that DTC movement is not cell autonomous.

A physical model for gonad morphogenesis

To better understand the physical mechanism by which the gonad elongates and turns, we modeled the gonad as an elastic cylinder of constrained diameter, with one end anchored to the spermatheca and uterus and the other capped by the DTC. We assumed the gonad to have an intrinsic elastic resistance to bending and to longitudinal compression/extension. Although *C. elegans* response to bending deformations has been shown to include a viscous component, the associated stress relaxation time is significantly shorter than the characteristic time of cell division in the gonad (Backholm et al., 2013). Similarly, it has been shown that viscous relaxation does not play a significant role in the mechanical response of *C. elegans* to compressive pressure beyond 100 s timescales (Gilpin et al., 2015), supporting the elastic treatment of the developing gonad. Further, we have taken into account the confinement of the gonad within the animal body by applying reflective boundary conditions representing the dorsal and ventral boundaries (STAR Methods; Figure S2). Because force equilibration within the system is assumed to occur at a faster timescale than the elongation of the gonad and the motion of the DTC (Bonnet et al., 2012; Khalilgharibi et al., 2019), the observed morphology of the gonad was taken to represent an equilibrium state. At each time point throughout development, the gonad shape was found by minimization of the total elastic energy of the system, which includes contributions from both bending and stretching/compression deformations of the gonad.

We simulated two alternative mechanistic scenarios for gonad development: one in which the DTC moves autonomously while pulling the gonad structure behind it (Figure 2A, top panel), and a proliferation-driven scenario in which the DTC is propelled by pushing forces produced by the proliferating germ cells within the gonad structure (Figure 2A, bottom panel). The essential difference between these scenarios is that the gonad bulk is under positive stress (i.e., stretched) for autonomous DTC motion (pulling by the DTC), while for proliferation-driven DTC motion (pushing the DTC) the gonad is under negative stress (i.e., compressed).

In the motile-DTC scenario, the positive elastic strain in the gonad bulk may be reduced by minimization of the overall gonad length. Prior to the DTC turn, such a length minimization is consistent with a straight gonad morphology. Following the turn, however, the retrograde motion of the DTC toward the gonad rear allows for a reduced overall gonad length. We found that under such conditions the equilibrium structures are cane-shaped, with a straight

(B) Maximum-intensity projection of an early L4-stage gonad expressing *lag-2p*::mNG::PH (cyan) and *pie-1p::mCherry::PH(PLC1delta1)* (pink).
(C) Phalloidin (gray) and DAPI (pink) stained L4-stage DTC expressing *lag-2p*::mNG::PH (cyan). Yellow arrows mark the germ cell nuclei, and asterisk shows the position of the DTC nucleus.
(D) Subcellular localization of Wrmscarlet-tagged LifeAct expressed under DTC-specific promoter, endogenously GFP-tagged CYK-1 (formin), and WVE-1 (WAVE ortholog) in the DTC. Yellow asterisk shows the position of the DTC nucleus.
(E) Cross-sectional view of the DTC during L4 stage, expressing NMY-2::mKate (pink), ARX-2::GFP (green), and GFP::WSP-1 (WASP ortholog). Pink arrows mark the rear end of the DTC, and yellow asterisk shows the position of the DTC nucleus.
(F) Representative confocal images of the germline (*pie-1p::mCherry::PH*(*PLC1delta1*, pink) and DTC (*lag-2p*::mNG::PH, cyan) in control worms (n = 86) and after DTC-specific depletion of NMY-2 (n = 65), ARX-2 (n = 50), and CYK-1 (n = 70).
(G) Representative confocal images of the DTC expressing NMY-2::mKate (pink) and ARX-2::GFP (green) in control, *nmy-2* (RNAi), and *arx-2* (RNAi) worms.
(H) Representative confocal images of the DTC expressing CYK-1::GFP (cyan) and ARX-2:: RFP (pink) in control and *cyk-1* (RNAi) worms.
(I–K) Quantification of NMY-2::mKate, ARX-2::GFP, and CYK-1::GFP intensity within the DTC in control (n = 14, 14, and 21) versus *nmy-2* (RNAi) (n = 20), *arx-2* (RNAi) (n = 19), and *cyk-1* (RNAi) worms (n = 22). Statistical analysis was carried out using the Mann-Whitney U test. "n" represents no. of gonads analyzed. Error bar denotes standard error of the mean (SEM), and all data are represented as mean ± SEM (**** $p < 0.0001$). Scale bars, 10 μm.

Please cite this article in press as: Agarwal et al., Directed cell invasion and asymmetric adhesion drive tissue elongation and turning in *C. elegans* gonad morphogenesis, Developmental Cell (2022), https://doi.org/10.1016/j.devcel.2022.08.003

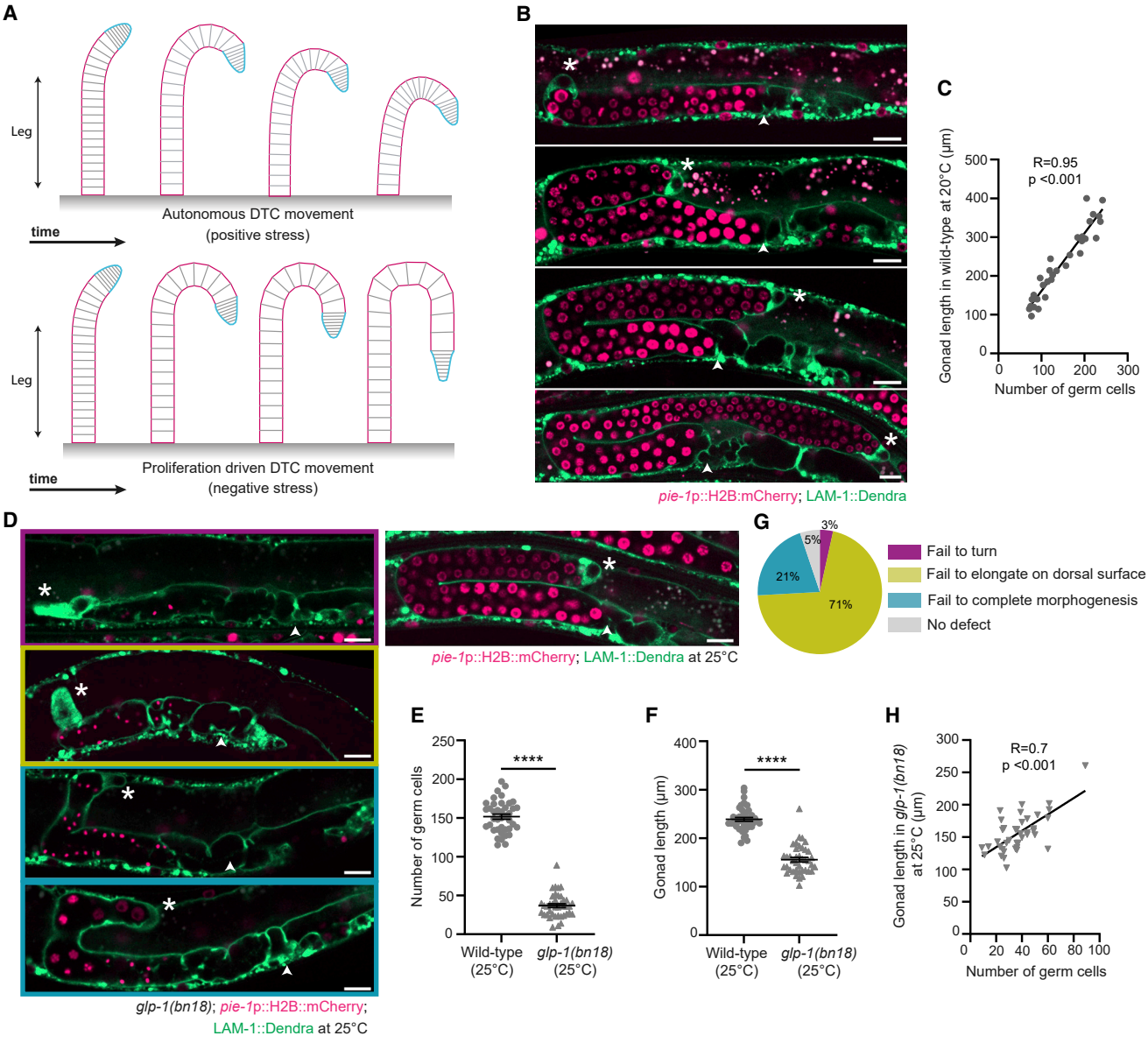

Figure 2. Germ cell proliferation is required for gonad elongation

(A) Simulations based on a qualitative physical model for gonad morphogenesis under the assumption of autonomous DTC movement (top) or proliferation-driven DTC movement (bottom). Pink curves represent the boundaries of the gonad bulk, and DTC cap is shown in cyan. Horizontal lines (gray) represent elastic constraint of the gonad diameter by sheath cells. The number of horizontal segments is constant throughout the simulation, such that reduction or increase in gonad length results in shorter or longer segments, respectively.

(B) Representative confocal images of the gonad in worms expressing a nuclear marker, mCherry::H2B (pink) and basement membrane marker, laminin-1::Dendra (green) during different developmental stages, from early L3 to late L4 stage (top to bottom), grown at 20°C. White asterisks indicate the distal end of the gonads and arrowheads mark its beginning.

(C) Correlation between gonad length and number of germ cells during different stages of gonad development in the wild-type worms grown at 20°C. R value indicates Pearson's correlation coefficient (n = 31).

(D) Representative confocal images of gonads expressing mCherry::H2B (pink) and laminin-1::Dendra (green) in control (rightmost image) versus *glp-1(bn18)* mutants (left panel) grown at the restrictive temperature of 25°C. White asterisks indicate the distal end of the gonads and arrowheads mark their beginning. Each dot within the *glp-1 (bn18)* gonads corresponds to a single sperm.

(E) Quantification of the number of germ cells in L4-stage wild-type gonads versus L4-stage *glp-1(bn18)* mutants grown at 25°C (n = 40).

(F) Quantification of the length of the L4-stage gonads in wild-type versus *glp-1(bn18)* mutants grown at 25°C (n = 40).

(G) Breakdown of gonad morphogenesis defects observed in *glp-1(bn18)* mutants grown at 25°C (n = 40). Phenotype color corresponds to the colored boxes in panel D.

(H) Correlation between gonad length and number of germ cells in *glp-1(bn18)* mutants grown at 25°C from larval stage 1 (L1). R value indicates Pearson's correlation coefficient (n = 40). Statistical analysis was carried out using the Mann-Whitney U test. "n" represents no. of gonads analyzed. Error bar denotes standard error of the mean (SEM), and all data are represented as mean ± SEM (**** $p < 0.0001$). Scale bars, 10 µm.

Please cite this article in press as: Agarwal et al., Directed cell invasion and asymmetric adhesion drive tissue elongation and turning in *C. elegans* gonad morphogenesis, Developmental Cell (2022), https://doi.org/10.1016/j.devcel.2022.08.003

"leg" that decreases in length as the DTC moves (Figure 2A, top panel). The autonomous DTC scenario is therefore inconsistent with the observed U-shape gonad morphology. In contrast, in the scenario in which the DTC is pushed forward by the negative longitudinal stress within the gonad bulk, our model predicts a U-shaped gonad that is consistent with the observed morphology in the adult worm (Figure 2A, bottom panel).

Proliferating germ cells drive gonad elongation

To explore the proliferation-driven gonad elongation model experimentally, we first counted the number of germ cells and measured the respective gonad length at different developmental time points. Longer gonads had a larger number of germ cells while shorter gonads had fewer germ cells, reflecting a strong positive correlation between germ cell number and gonad length (Figures 2B and 2C). To test whether proliferation is required for gonad morphogenesis, we reduced germ cell proliferation by employing a temperature-sensitive *glp-1(bn18)* mutant. GLP-1 is a transmembrane receptor expressed in germ cells that is required for Notch signaling and is crucial for germ cell proliferation (Kimble, 2005). At the restrictive temperature of 25°C, *glp-1(bn18)* mutants have on average 24% of wild-type number of germ cells, and they all prematurely differentiate into sperm (Figures 2D and 2E). Consequently, the length of *glp-1(bn18)* mutant gonads was significantly reduced (61% of wild type, Figure 2F) and 3% of them failed to turn, 71% did not reach the dorsal side, and 21% of gonads were unsuccessful in developing the complete U-shaped architecture (Figure 2G). Nevertheless, we observed a strong correlation between the gonad length and germ cell number in *glp-1(bn18)* mutants, as seen in the control (Figure 2H). Complete removal of germ cells is technically challenging, as the signals from the sheath cells that support mitosis are not known. Taken together, these results indicate that germ cell proliferation plays a crucial role in gonad elongation.

The DTC is under pressure, which is released by matrix degradation

To directly test whether the DTC is under pressure from inside the gonad we performed laser microsurgery experiments in conjunction with live imaging. Two simultaneous ablations of the basement membrane on either side of the DTC near its rear end caused a rapid forward displacement of the DTC by 1.6 ± 0.3 μm (n = 11) within a duration of 6–8 s (Figures 3A and 3B; Video S1). This magnitude of DTC displacement is extraordinary, considering the known rate of DTC migration is 12.15 ± 1.84 μm/h (Berger et al., 2018), suggesting that the proliferating germ cells exert a constant pushing force, which is resisted by the basement membrane and DTC. Moreover, the brief duration of the displacement step is consistent with the timescale for relaxation of stresses in epithelial tissues (Chaudhuri et al., 2020; Khalilgharibi et al., 2019). Because the DTC is a 3D structure, it should remain in partial contact with the germ cells even after the two-sided ablations. Nevertheless, to rule out the possibility of complete detachment of the DTC from the gonad, we carried out laser ablation on only one side of the DTC and observed a similar instantaneous forward movement (Figure S3; Video S2). These results indicate that the post-ablation DTC movement results from rapid relaxation of stress following disruption of the confining basement membrane. We further confirmed the existence of pressure within the gonad by making a laser incision at loop region of the gonad, away from the DTC (Figure 3C). After ablation, germ cell nuclei moved quickly toward the incision site indicating a release of pressure (Figures 3C and 3D; Video S3). A similar displacement of germ cell nuclei was observed after the laser ablation at the DTC tip (Figure S4; Video S4). To investigate whether this pressure is dependent on germ cell proliferation, we examined pressure within the proliferation-defective *glp-1(bn18)* gonads at the restrictive temperature of 25°C. Contrary to the control, the DTC in *glp-1(bn18)* mutants failed to show any significant forward displacement following laser ablation on two sides, suggesting that the gonadal pressure is proliferation-dependent (Figures 3E and 3F; Video S5).

Next, we hypothesized that a gradual and localized release of this pressure at the DTC front, caused by metalloprotease-mediated matrix degradation, leads to forward DTC movement and gonad elongation (Figure 4A). To test this hypothesis, we first examined the subcellular localization of endogenously mNeonGreen (mNG)-tagged GON-1, an ortholog of the vertebrate ADAMTS family of matrix metalloproteases (Llamazares et al., 2003; Somerville et al., 2003). GON-1 is expressed in the DTCs and muscle cells and facilitates gonad expansion and morphogenesis (Blelloch et al., 1999; Blelloch and Kimble, 1999; Nishiwaki et al., 2000). Consistent with our hypothesis, we found a strong enrichment of GON-1::mNG at the tips of the DTCs at different stages of gonad development (Figure 4B). Furthermore, GON-1 depletion by RNAi caused a strong accumulation of a basement membrane component, laminin, specifically around the DTC (Figures 4C and 4D), suggesting that GON-1 cleaves laminin to enable forward motion of the DTC tip. We further analyzed the dynamics of laminin-1::Dendra at the DTC tip versus a proximal region of the gonad using fluorescence recovery after photobleaching (FRAP). We observed a significantly larger mobile fraction of laminin-1::Dendra at the DTC tip (26.7% ± 1.7%) than at the proximal region of the gonad (11% ± 0.68%) (Figures 4E–4G; Video S6). Thus, it suggests that the basement membrane is more dynamic at the DTC tip as compared with the other regions of the gonad. Finally, consistent with previous studies (Blelloch et al., 1999; Blelloch and Kimble, 1999; Nishiwaki et al., 2000), DTC-specific depletion of GON-1 resulted in a disorganized gonad morphology with short but broad gonads having a large number of germ cells expanding in all directions within the worm body (Figures 4H and 4I). These results show that the directionality of gonad elongation is provided by DTC-enriched secretion of the metalloprotease GON-1, which degrades the matrix in front, leading to a directional release of proliferative pressure.

Together, the results shown in Figures 2, 3, and 4 indicate that the gonad elongates not by a pulling force caused by active DTC migration but rather due to the pushing force generated by confined proliferating germ cells behind the DTC, accompanied by a gradual and directed release of pressure in the front due to DTC-generated matrix degradation (Figure 4A). With this mechanism in mind, we next explored the process of DTC and gonad turning.

Please cite this article in press as: Agarwal et al., Directed cell invasion and asymmetric adhesion drive tissue elongation and turning in *C. elegans* gonad morphogenesis, Developmental Cell (2022), https://doi.org/10.1016/j.devcel.2022.08.003

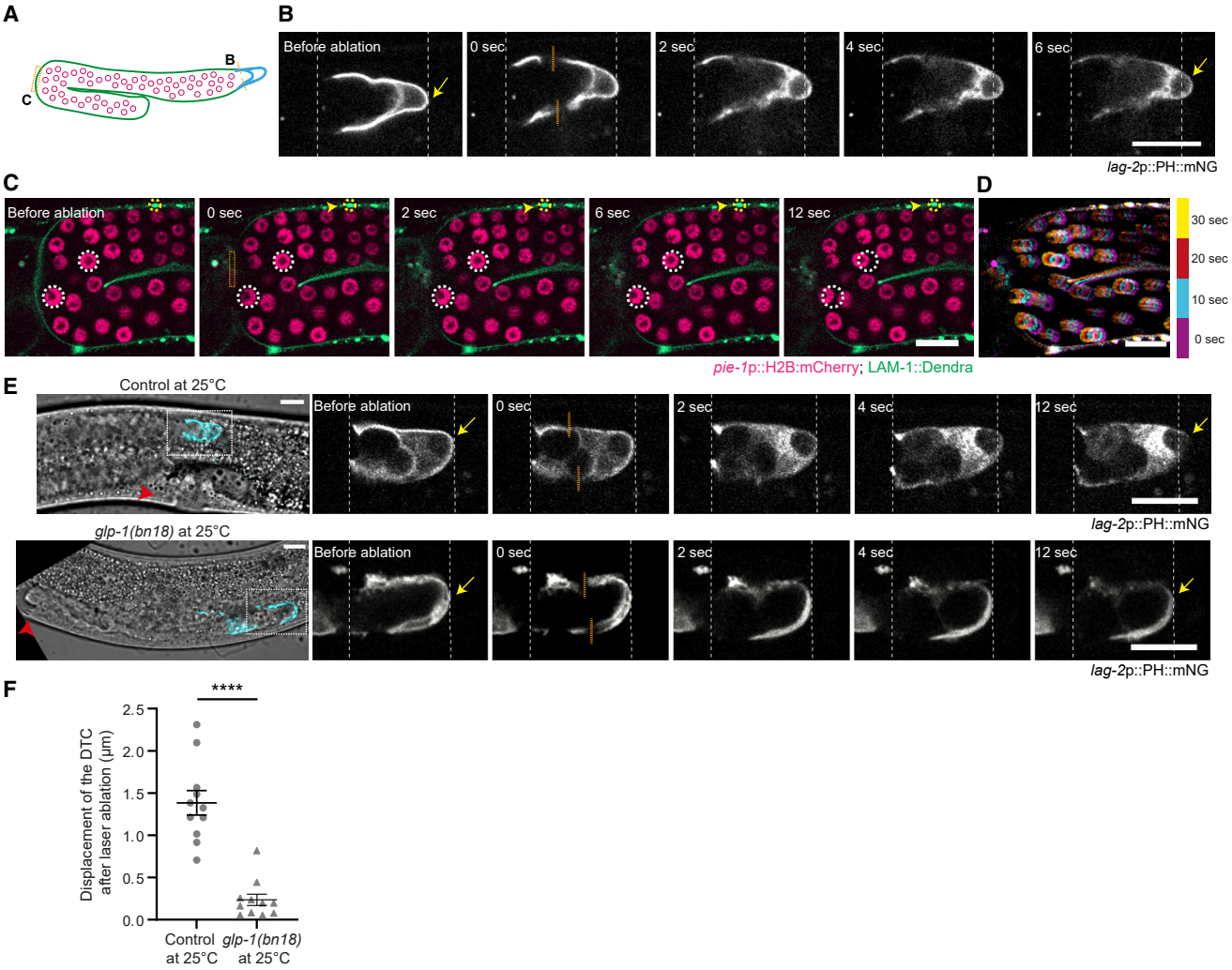

Figure 3. Pushing force generated by germ cell proliferation, within a confined basement membrane, elongates the *C. elegans* gonad

(A) Schematic of a gonad depicting the regions of laser ablation (orange dotted lines) carried out for the experiments shown in (B) and (C). Green outline shows basement membrane, pink circles are the germ cell nuclei, and cyan cap depicts the DTC.

(B) Time-lapse images of a DTC expressing *lag-2p*::mNG::PH after two simultaneous laser incisions were made at its rear end (marked with two orange lines). Two dotted lines and the yellow arrow show the position of the DTC before and after the laser ablation.

(C) Time-lapse images of a gonad expressing a nuclear marker (mCherry::H2B, pink) and basement membrane marker (laminin-1::Dendra, green) after a laser incision at the loop region (marked with an orange rectangular box). White dotted circles show the displacement of two germ cell nuclei after the laser ablation. Yellow arrowhead and a dotted circle mark a high-intensity fluorescent particle showing no displacement of the worm with time.

(D) Movement of the germ cell nuclei and basement membrane after laser ablation at the loop region, visualized by pseudo-coloring each time point as indicated.

(E) Nomarski images show the gonad expressing *lag-2p*::mNG::PH, a DTC membrane marker, in control (top panel) versus *glp-1(bn18)* mutants at 25°C (bottom panel). Red arrowheads indicate the position of vulva. Fluorescent time-lapse images show the DTC after two simultaneous laser incisions were made (marked with two orange lines) at the rear end. Two dotted lines and yellow arrow indicate the position of DTC before and after the laser ablation.

(F) Quantification of the DTC displacement 10 s after the laser ablation (as shown in figure in E) in control (n = 11) versus *glp-1(bn18)* mutants (n = 11) at 25°C. Statistical analysis was carried out using Mann-Whitney U test. "n" represents no. of gonads analyzed. Error bar denotes standard error of the mean (SEM) and all data are represented as mean ± SEM (**** $p < 0.0001$). Scale bars, 10 µm.

Polarized DTC-ECM adhesion regulates gonad turning

Based on our proliferation-driven DTC model, we hypothesized that the turning of the DTC may be achieved by forming asymmetrical DTC-extracellular matrix (ECM) adhesions. The pushing force exerted by the gonad bulk, together with the force exerted by the localized adhesions, would result in a net moment that acts to rotate the DTC about the highly adhering region. Once a complete about-turn is effected, a symmetrical redistribution of the DTC-ECM adhesions will end the DTC rotation (Figure 5A).

To explore these predictions, we first analyzed the localization of endogenously tagged cell-matrix adhesion receptors, a β-integrin (PAT-3) and an α-integrin subunit (INA-1) (Baum and Garriga, 1997; Gettner et al., 1995; Meighan and Schwarzbauer, 2014), in the DTC. We observed a uniform distribution of PAT-3 and INA-1 in the DTC when the gonad elongated in a straight

Please cite this article in press as: Agarwal et al., Directed cell invasion and asymmetric adhesion drive tissue elongation and turning in *C. elegans* gonad morphogenesis, Developmental Cell (2022), https://doi.org/10.1016/j.devcel.2022.08.003

CellPress

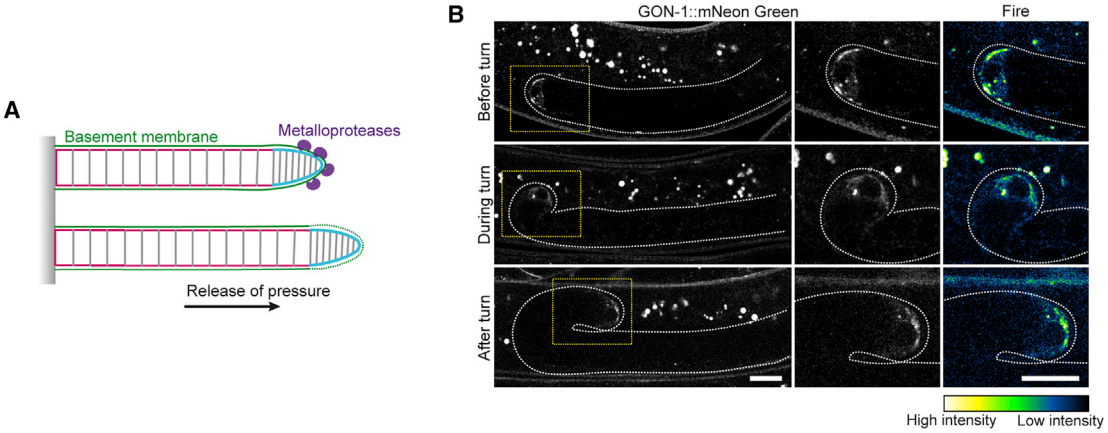

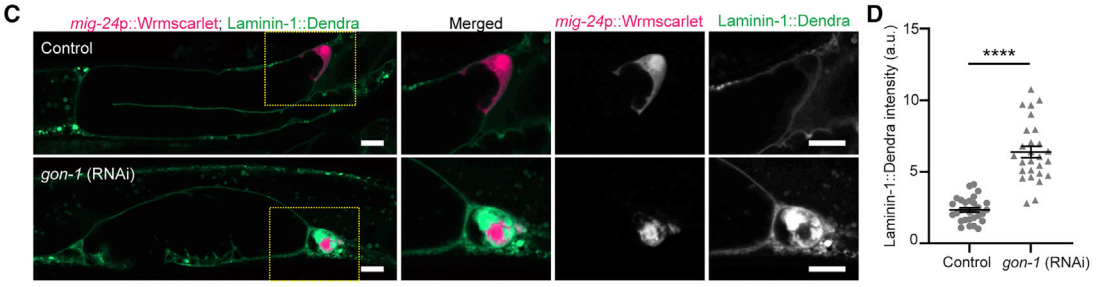

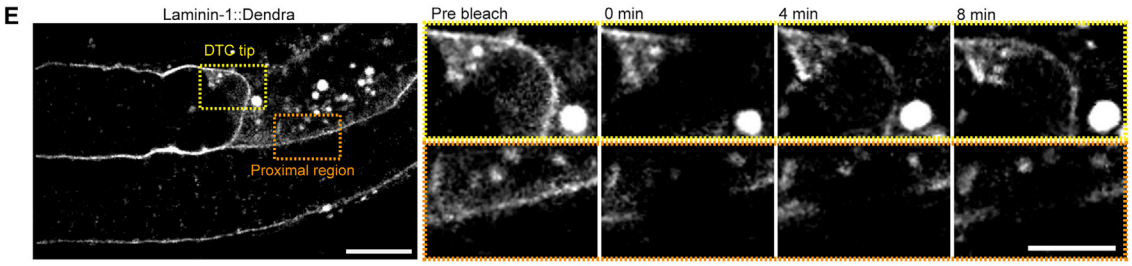

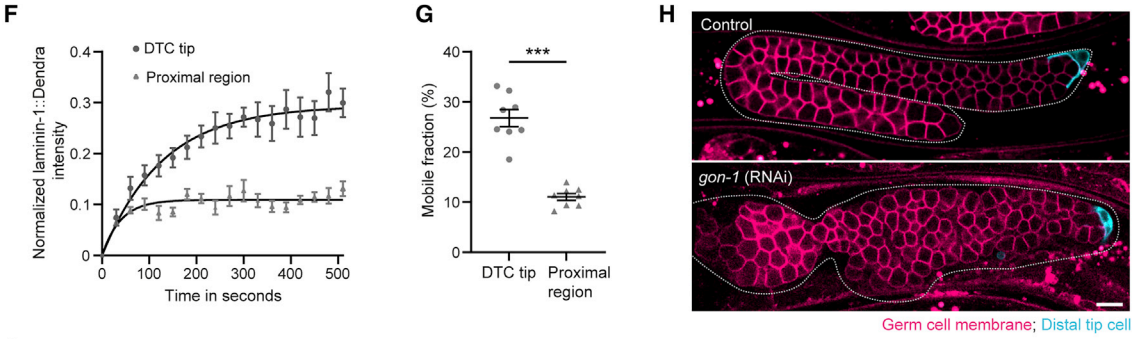

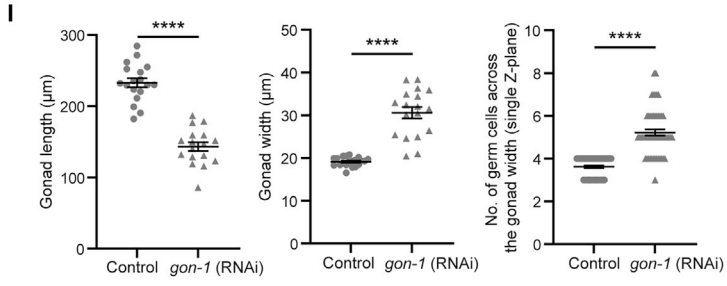

(legend on next page)

Please cite this article in press as: Agarwal et al., Directed cell invasion and asymmetric adhesion drive tissue elongation and turning in *C. elegans* gonad morphogenesis, Developmental Cell (2022), https://doi.org/10.1016/j.devcel.2022.08.003

line on both the ventral and dorsal surfaces; however, during the turn, PAT-3::GFP and INA-1::mNG were asymmetrically distributed, showing a strong enrichment along the dorsal side of the cell (Figures 5B–5E). Talin, a cytoskeletal protein that links integrins to the actin cytoskeleton, is a marker for activated integrins (Critchley, 2005; Shattil et al., 2010). We found that the *C. elegans* ortholog of Talin, TLN-1 (Cram et al., 2003; Moulder et al., 1996), was also asymmetrically enriched on the dorsal surface of the DTCs during the turn, similar to the integrin subunits (Figures 5F and 5G). In contrast, a neutral plasma membrane marker (mCherry::PH(PLC1delta1)) did not show any dorsoventral polarity during the turn (Figure S5). The average membrane intensity of GFP::PAT-3, INA-1::mNG, and GFP::TLN-1 remained unaltered before, during, and after the DTC turn (Figure S6). These observations were consistent with the idea that polarized DTC-ECM adhesion could be driving the gonad U-turn.

Next, we simulated the effects of adhesion strength and distribution asymmetry on gonad morphology in the proliferation-driven model. We treated the DTC cell-matrix interaction as stick-slip friction (Aratyn-Schaus and Gardel, 2010; Chan and Odde, 2008) by modeling adhesions as linear springs that can support a maximal strain before disengaging (Shemesh et al., 2012). The strength of the adhesions is therefore characterized by an effective spring constant, $\tilde{k}$ (see STAR Methods section for more detail). Further, we studied the role of asymmetrical adhesion distribution in the DTC by varying the duration at which asymmetric adhesions are maintained. We calculated the equilibrium morphologies for gonads elongating to twice their initial length. We defined f_{as} as the fraction of time at which asymmetric adhesions are applied, where 0 corresponds to a case where no uneven adhesion distribution occurs and 1 represents a scenario in which uneven adhesion distribution is constantly maintained. The calculated positions of the DTC relative to the gonad rear, as well as the orientation angles of the DTC relative to the animal's longitudinal axis, are presented in Figure 6A. We found that the "U-shape" phenotype was reached for a range of system parameters (see * in Figure 6A). For weak and short-lived adhesions (low $\tilde{k}$and f_{as}), the DTC failed to complete the turn, resulting in an "S-shape" morphology (see † in Figure 6A). Conversely, overly strong adhesions applied for longer times (large $\tilde{k}$ and f_{as}) resulted in a "snail-shape" morphology (see ‡ in Figure 6A).

We performed genetic manipulations that weaken or increase adhesion to test the predictions of the model. As predicted by our simulation and reported in previous studies (Baum and Garriga, 1997; Cram et al., 2006, 2003; Lee et al., 2001a; Meighan and Schwarzbauer, 2007; Wong et al., 2014), DTC-specific depletion of PAT-3, INA-1, and TLN-1 caused turning defects (14.6%, 32%, and 36%, respectively) with "S-shaped" gonads elongating on the dorsal surface away from the midbody rather than toward it (Figures 6B and 6D). To extend the duration of adhesion, we depleted the transcription factor VAB-3/PAX-6, which has been shown to be required for downregulation of INA-1 (Cram et al., 2006; Meighan and Schwarzbauer, 2007). Consistent with these studies, DTC-specific depletion of VAB-3 resulted in snail-shaped gonads (Figures 6C and 6D). As expected, VAB-3 knockdown caused a significant increase in the intensity of mNeon green-tagged INA-1 in the DTC (Figures 6E and 6F). Taken together, these results indicate that gonad turning is triggered by the asymmetric concentration of cell-matrix adhesions on the dorsal side of the DTC. Thus, we next explored the signaling molecules responsible for this adhesion polarity.

CDC-42, SRC-1, and netrin signaling regulate DTC-ECM adhesion polarity during gonadal turn

We found Rho GTPase CDC-42 (Etienne-Manneville, 2004), a well-conserved cell polarity regulator across multiple species (Etienne-Manneville, 2004; Pichaud et al., 2019), including *C. elegans* (Abrams and Nance, 2021; Gotta et al., 2001; Kay and Hunter, 2001; Marston et al., 2016; Rohrschneider and Nance, 2009), and Src family tyrosine kinase SRC-1 (Itoh et al., 2005; Playford and Schaller, 2004) to be required for integrin polarity. RNAi depletion of either CDC-42 or SRC-1 diminished the gradient of PAT-3::GFP intensity in the turning DTC, although *src-1* (RNAi) had a much stronger effect than *cdc-42* (RNAi), with more evenly distributed PAT-3::GFP in the DTC (Figures 7A and 7B). Consistently, DTC-specific knockdown of CDC-42 or SRC-1 resulted in gonads that either failed to turn or turned away from the midbody (Figure 7C). Turning defects were observed approximately twice as often in *src-1* (RNAi) (47% turn defect) as in *cdc-42* (RNAi) (21% turn defect). These results further support differential DTC-ECM adhesion as a mechanism driving gonad turning and establish SRC-1 and CDC-42 as upstream regulators.

Figure 4. Localized release of pressure at the DTC tip via GON-1, a matrix metalloprotease, leads to gonad elongation

(A) Schematic showing the proposed mechanism of gonad elongation by proliferative pressure. Proliferative pressure within the gonad is resisted by a basement membrane (green) surrounding the gonad and DTC. At the front of the gonad, the DTC secrets metalloproteases (purple) that degrade the matrix and thus provide an outlet for the release of pressure and forward DTC movement.

(B) Localization of endogenously mNeon-Green-tagged GON-1 in the DTC before, during, and after the turn. Magnified views of the regions marked by dotted yellow boxes are also shown. Left panel, grayscale images; right panel, corresponding "fire" look-up table (LUT) images.

(C) Representative confocal images of the gonad expressing basement membrane marker, laminin-1::Dendra (green) and a DTC marker, *mig-24*p::WrmScarlet (pink) in control worms and after depletion of GON-1.

(D) Quantification of Laminin-1::Dendra intensity within the DTC in control (n = 30) versus *gon-1* (RNAi) (n = 27).

(E) Representative time-lapse images of a gonad expressing Laminin-1::Dendra before and after photobleaching of the Laminin-1::Dendra at the DTC tip (yellow dotted box) and proximal region of the gonad (orange dotted box) (n = 8).

(F and G) Quantification of the recovery kinetics and percentage of mobile fraction of the Laminin-1::Dendra analyzed after photobleaching at the DTC tip and proximal region of the gonad (n = 8).

(H) Representative confocal images of the germline (*pie-1p::mCherry::PH(PLC1delta)*, pink) and DTC (*lag-2p*::mNG::PH, cyan) in control worms and after DTC-specific depletion of the metalloprotease GON-1.

(I) Quantification of gonad length, gonad width, and the number of germ cells across the width of the gonad in control (n = 18, 20, and 20) versus *gon-1* (RNAi) worms (n = 17, 18, and 18). Statistical analysis was carried out using Mann-Whitney U test. "n" represents no. of gonads analyzed. Error bar denotes standard error of the mean (SEM), and all data are represented as mean ± SEM (**** $p < 0.0001$, *** $p < 0.001$). Scale bars, 10 μm.

Please cite this article in press as: Agarwal et al., Directed cell invasion and asymmetric adhesion drive tissue elongation and turning in *C. elegans* gonad morphogenesis, Developmental Cell (2022), https://doi.org/10.1016/j.devcel.2022.08.003

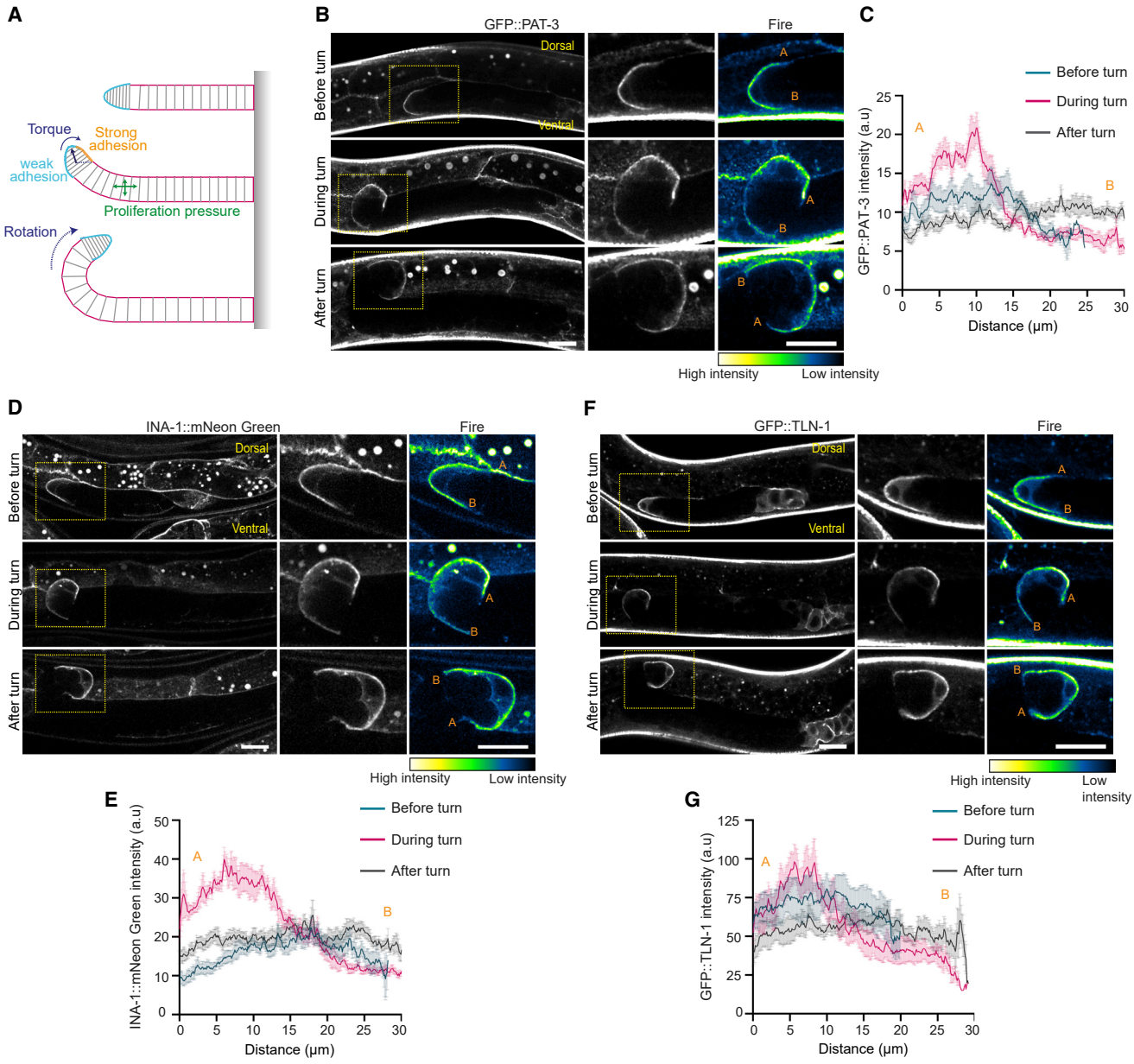

Figure 5. Polarized enrichment of cell-matrix adhesion in the DTC during the turn

(A) Schematic representation of a qualitative physical model explaining the mechanism of DTC turning. Polarized enrichment of cell-matrix adhesion (orange region) (stronger on the dorsal side of the DTC than the ventral side) along with the proliferative pushing force (green arrows) coming from behind the DTC generates a torque (blue), and the DTC (cyan) rotates around the strong cell-matrix adhesion site.

(B and C) Representative confocal images of the DTC expressing GFP::PAT-3 and GFP::PAT-3 membrane intensity profiles before, during, and after the DTC turn (n = 10), respectively.

(D and E) Representative confocal images of the DTC expressing INA-1::mNeon Green and INA-1::mNeon Green (mNG) membrane intensity profiles before, during, and after the DTC turn (n = 11), respectively.

(F and G) Representative confocal images of the DTC expressing GFP::TLN-1 and GFP::TLN-1 membrane intensity profiles before, during, and after the DTC turn, respectively (n = 10). In each image, magnified views of the regions marked by dotted yellow boxes are also shown. Left panel, grayscale images; right panel, corresponding fire look-up table (LUT) images. Intensity was measured by tracing a 7-pixel-wide line along the DTC membrane, from the dorsal end (point A) to the ventral end (point B). "n" represents no. of gonads analyzed. Error bar denotes standard error of the mean (SEM), and all data are represented as mean ± SEM. Scale bars, 10 μm.

Netrin signaling has been shown to guide the DTC toward the dorsal surface and away from the ventral surface (Chan et al., 1996; Hedgecock et al., 1990; Leung-Hagesteijn et al., 1992). Interestingly, SRC-1 was found to be downstream of the netrin receptor UNC-5 (Lee et al., 2005). We therefore explored whether netrin signaling might control asymmetric integrin

Please cite this article in press as: Agarwal et al., Directed cell invasion and asymmetric adhesion drive tissue elongation and turning in *C. elegans* gonad morphogenesis, Developmental Cell (2022), https://doi.org/10.1016/j.devcel.2022.08.003

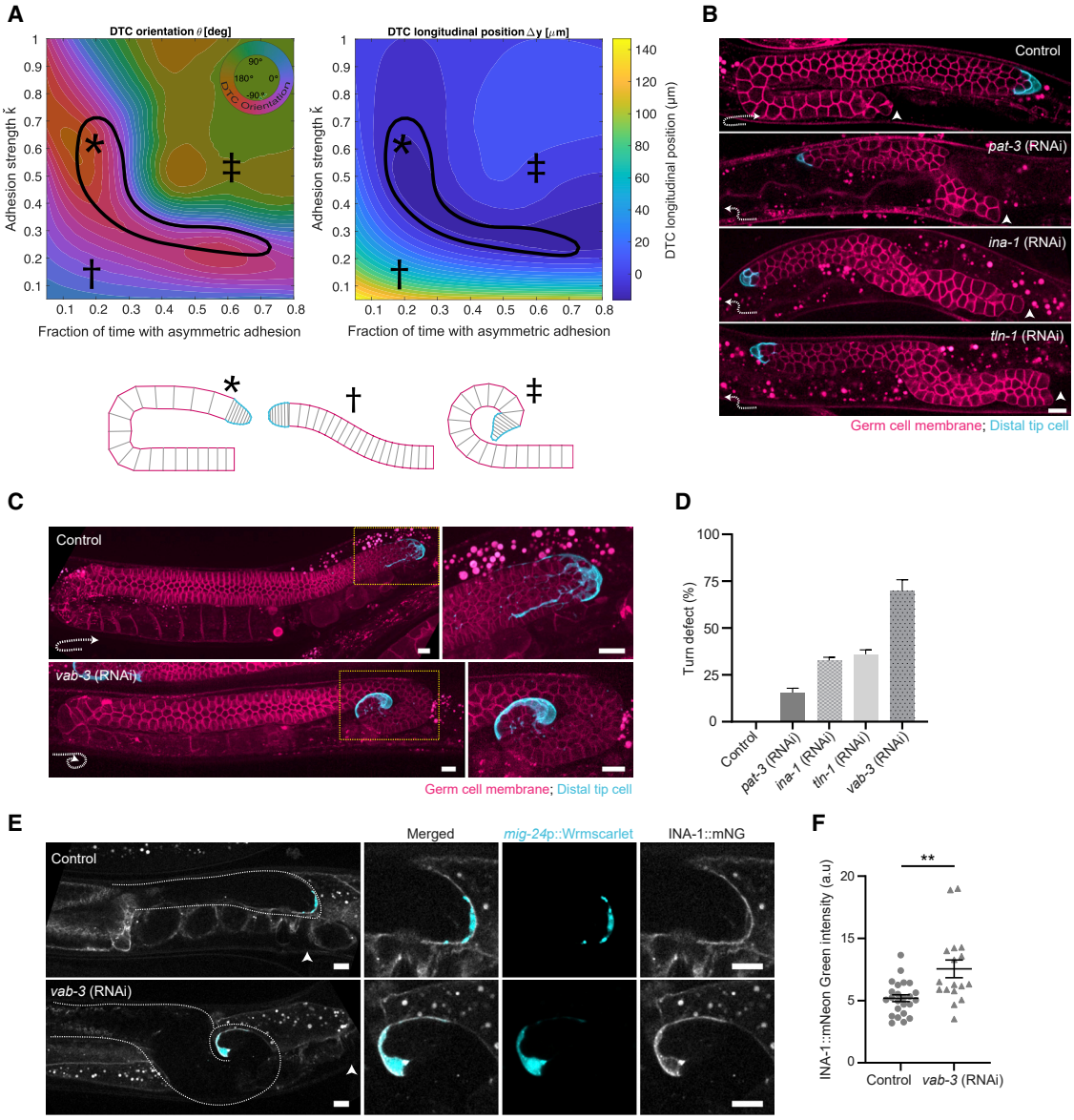

Figure 6. Polarized enrichment of cell-matrix regulates DTC turn

(A) Phase diagram showing the effect of various combinations of adhesion strength (y axis) and duration of asymmetric adhesion (x axis) on the final morphology of the gonad, based on numerical simulations. The left panel indicates the longitudinal position of the DTC, Δy, measured from the rear. The right panel indicates θ, the angle between the longitudinal body axis and the direction of DTC orientation. The orientation angle is defined such that $\theta = 0°$ corresponds to the pre-turn direction of DTC motion, while $\theta = \pm 180°$ corresponds to the opposite orientation toward the rear. Negative θ values designate DTCs oriented in the dorsal direction, while positive values indicate the basal direction. The region of the phase diagram at which $\Delta y \leq 0$ and $|\theta| \geq 135°$ (i.e., DTC has reached the rear anchoring and is oriented backward) is defined as a successful turn with normal morphology (interior of black curve). Three architypes of phenotypes (shown at bottom) are marked in the diagram: asterisk (*) indicates the conditions in which the gonad forms normal U-shaped architecture. (‡) indicates too-strong adhesions for a very long period that leads to a snail-shaped turn. Contrarily, (†) indicates weak adhesions for a short period that result in a "flat S" shaped phenotype.

(B) Representative confocal images of the larval germline (*pie1p::mCherry::PH(PLC1delta1)*), pink) and DTC (*lag-2p*::mNG::PH, cyan) in control worms and after DTC-specific depletion of β-integrin (PAT-3), α-integrin (INA-1), and Talin (TLN-1). White arrowheads indicate the beginning of the gonads.

(C) Representative confocal images of the adult germline (*pie1p::mCherry::PH(PLC1delta1)*, pink) and DTC (*lag-2p*::mNG::PH, cyan) in control worms and after DTC-specific depletion of a transcription regulator, VAB-3/PAX-6. Magnified views of the regions marked by dotted yellow boxes are also shown.

(D) Percentage of turn defects observed after DTC-specific depletion of PAT-3 (n = 41), INA-1 (n = 69), TLN-1 (n = 67), and VAB-3 (n = 80).

(E) Representative confocal images of the adult gonad expressing INA-1::mNG (gray) and *mig-24*p::Wrmscarlet (cyan), a DTC marker in control and *vab-3* (RNAi) worms. Magnified images of the DTC are shown on the right.

(F) Quantification of INA-1::mNG intensity within the DTC in control (n = 24) versus *vab-3* (RNAi) (n = 17). Statistical analysis was carried out using the Mann-Whitney U test. "n" represents no. of gonads analyzed. Error bar denotes standard error of the mean (SEM) and all data are represented as mean ± SEM (** $p < 0.005$). Scale bars, 10 μm.

Please cite this article in press as: Agarwal et al., Directed cell invasion and asymmetric adhesion drive tissue elongation and turning in *C. elegans* gonad morphogenesis, Developmental Cell (2022), https://doi.org/10.1016/j.devcel.2022.08.003

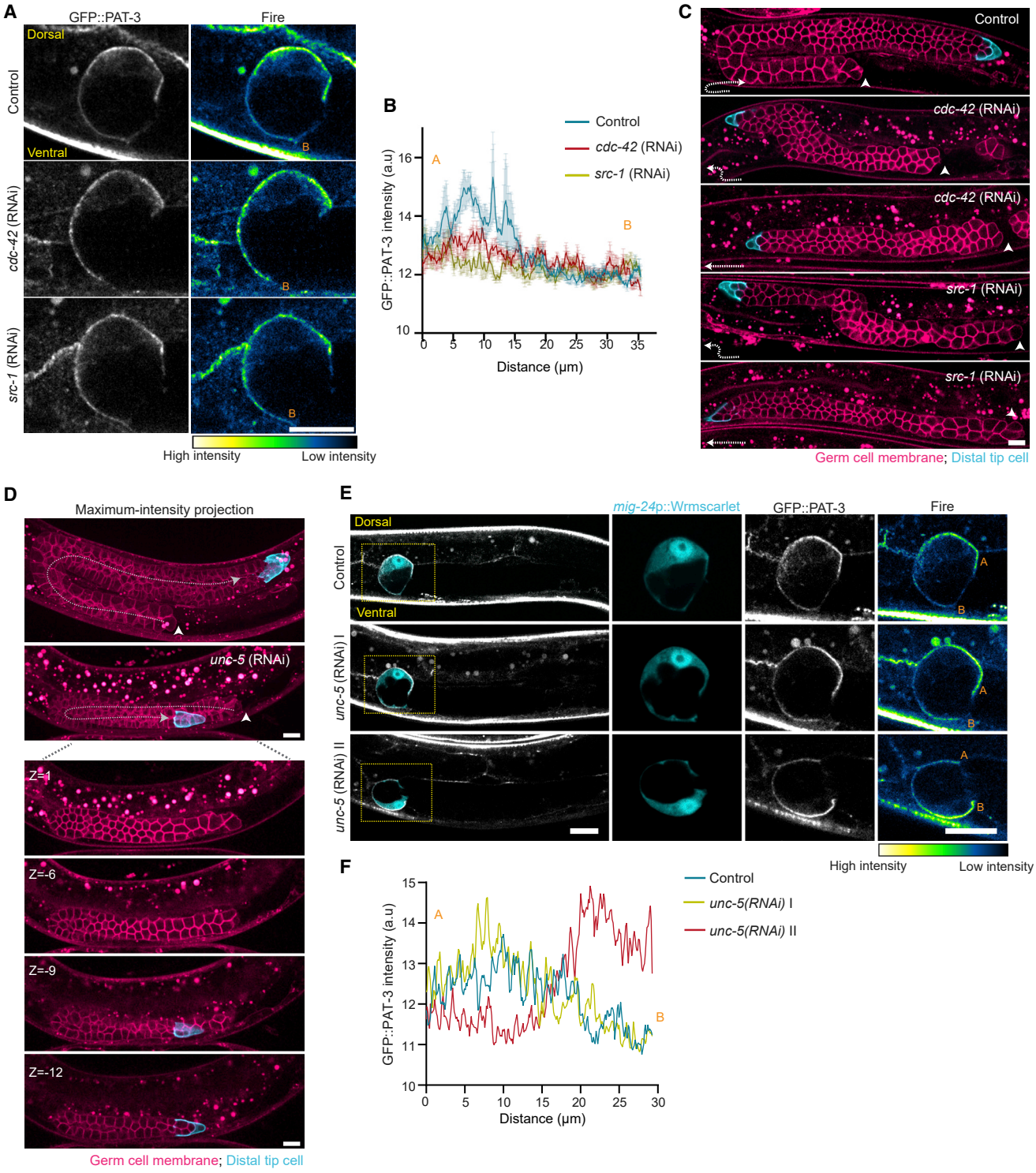

Figure 7. Role of CDC-42, SRC-1, and netrin signals in regulating integrin polarity during DTC turn

(A) Representative confocal images of GFP::PAT-3 distribution within the DTC after knockdown of CDC-42 and SRC-1 (left panel, grayscale images; right panel, corresponding fire look-up table [LUT] images).

(B) GFP::PAT-3 membrane intensity profile distribution during DTC turn in control, *cdc-42* (RNAi), and *src-1* (RNAi) worms (n = 8 for each).

(C) Representative confocal images of the germline (*pie-1p::mCherry::PH(PLC1delta1)*), pink) and DTC (*lag-2p*::mNG::PH, cyan) in control worms and after DTC-specific depletion of the RhoGTPase CDC-42 (n = 135) and Src family tyrosine kinase SRC-1 (n = 57). White arrowheads indicate the beginning of the gonads.

(D) Maximum-intensity projected confocal images of gonads observed in control and *unc-5* (RNAi) worms. Bottom panel, z stacks of *unc-5* (RNAi) gonad from top to bottom, each with a z-plane spacing of 1 μm.

(legend continued on next page)

Please cite this article in press as: Agarwal et al., Directed cell invasion and asymmetric adhesion drive tissue elongation and turning in *C. elegans* gonad morphogenesis, Developmental Cell (2022), https://doi.org/10.1016/j.devcel.2022.08.003

localization via UNC-5 and SRC-1 and in that way induce turning. We performed DTC-specific knockdown of UNC-5 and examined PAT-3:GFP distribution during the turn and final gonad morphology. Consistent with previous reports (Hedgecock et al., 1990; Su et al., 2000), UNC-5 depleted DTCs failed to turn toward the dorsal surface. However, DTC turning per se was unaffected, as was DTC adhesion polarity. After completing a U-turn, the gonads continued to elongate on the ventral surface, instead of the dorsal surface, toward the midbody (Figure 7D). Interestingly, the ventralized *unc-5* (RNAi) gonads could be formed by either a rightward or leftward turn of the DTC. In both cases, they exhibited a polar distribution of PAT-3 and, importantly, in each case the high PAT-3::GFP intensity was localized at the inside of the turn (Figures 7E and 7F). This finding further strengthens our hypothesis that the DTC steers the motion of the elongating gonad by selectively forming cell-matrix adhesions in the direction of the turn, and it shows that netrin signaling functions to orient the axis of DTC rotation and that cell-matrix adhesions polarize along this axis.

DISCUSSION

Previously published forward and reverse genetic screens have identified numerous genes that play a role in gonad morphogenesis, including genes involved in temporal regulation, cell fate determination, signaling, trafficking, cell-matrix adhesion, and ECM remodeling (Cram et al., 2006; Hedgecock et al., 1990; Itoh et al., 2005; Lee et al., 2001b; Nishiwaki, 1999; Nishiwaki et al., 2000; Reddien and Horvitz, 2000; Tannoury et al., 2010). Current models assume that gonad development is predominantly driven by active DTC movement, with a possible role for germ cell proliferation (Atwell et al., 2015; Cecchetelli and Cram, 2017; Killian and Hubbard, 2005; Kimble and White, 1981; Sherwood and Plastino, 2018; Wong and Schwarzbauer, 2012). In contrast, we show that the DTC is not self-propelled but rather pushed by the proliferating germ cells. Although the DTC propulsion force is external in nature, our findings demonstrate that the DTC does not serve a merely passive role in gonad morphogenesis. Rather, it actively directs the direction of elongation by controlled and timely interactions with the surroundings. We characterize these interactions and elucidate the cellular mechanisms used by the DTC to govern gonad elongation and turning.

Tissue elongation can be achieved via cell migration, intercalation, cell shape changes, and oriented cell divisions (Andrew and Ewald, 2010). Lack of any protrusions at the leading edge of the DTC and the dispensability of force-generating machinery components for the DTC movement (Figure 1) ruled out the possibility of active cell migration as a mechanism for *C. elegans* gonad elongation. Tissue extension by cell intercalation involves cell rearrangement, leading to tissue shape deformation—for example, during the embryonic development of *Drosophila*, the germ band extends along anterior-posterior axis and converges along the dorsoventral axis (Tetley and Mao, 2018; Walck-Shannon and Hardin, 2014). Although the *C. elegans* gonad elongates along the antero-posterior axis, it does not reduce its diameter; in fact it becomes wider, ruling out convergent extension as a mechanism (Atwell et al., 2015; Pazdernik and Schedl, 2013). Previous studies have shown that the dividing germ cells present behind the DTC have randomly oriented mitotic spindles (Crittenden et al., 2006; Gordon et al., 2020), thus eliminating the possibility of oriented cell divisions as a mechanism for gonad elongation. Here, we reveal a distinct mechanism of organ elongation, driven by proliferative pressure due to confinement by a basement membrane envelope, which is released locally by matrix degradation via secretion of metalloproteases by the leader cell (Figures 2, 3, and 4). Localized breaching of basement membrane integrity is involved in the shaping of various organs (Crest et al., 2017; Harunaga et al., 2014; Kyprianou et al., 2020), yet the role of proliferative pressure remained unexplored. An analogy can be drawn between how the DTC guides follower germ cells for tissue morphogenesis and how cancer-associated fibroblasts (CAFs) create tracks by matrix remodeling for cancer cell invasion (Gaggioli et al., 2007). Whether mechanical force, such as that caused by proliferative pressure, induces the local release of metalloproteases for matrix remodeling is of interest for future studies. The role of pressure in tissue morphogenesis is well exemplified by a recent study showing that osmotic pressure derived from swelling of extracellular hyaluronate shapes epithelial buds into tubes during zebrafish ear morphogenesis (Munjal et al., 2021).

Although the effects of mechanical forces on cell proliferation and tissue morphogenesis have now been extensively described, the origins of such forces are usually attributed to intracellular molecular motors. Our findings demonstrate that cell proliferation can, in itself, provide the mechanical work to propel the developmental process. This mechanism of directed invasion likely plays a role in the development of other organs, such as kidneys and salivary glands, and may also be relevant for solid tumor metastasis.

Noteworthy, the DTC serves as a germ cell niche, signaling through Notch to induce the proliferation of the germ cells behind it. This means that the DTC contributes to its own propulsion, albeit indirectly. During gonad development, there is no loss of germ material from the proximal end and the increase in germ cell numbers contribute to gonad elongation. Once gonad morphogenesis is complete, the exit of oocytes ovulating through the spermatheca, as well as apoptosis and engulfment of germ cells along the U-turn, could balance the proliferation in the distal end so that the length of the gonad would remain constant. Our current model for gonad elongation requires proliferative pressure and a concomitant release of this pressure by matrix degradation at the DTC tip via metalloproteases such as GON-1. We hypothesize that GON-1 secretion is

(E) Two different representative confocal images of the *unc-5* (RNAi) ventralized DTCs expressing GFP::PAT-3 (gray) and *mig-24*p::Wrmscarlet (cyan), a DTC marker. Magnified views of the regions marked by dotted yellow boxes are also shown. Left panel, grayscale images; right panel, corresponding fire look-up table (LUT) images.

(F) GFP::PAT-3 intensity profile distribution along the DTC membrane during the turn in control and *unc-5* (RNAi) worms (measured from the images shown in panel E). Intensity was measured by tracing a 7-pixel-wide line along the DTC membrane, from the dorsal end (point A) to the ventral end (point B). "n" represents no. of gonads analyzed. Error bar denotes standard error of the mean (SEM), and all data are represented as mean ± SEM. Scale bars, 10 μm.

terminated in the adult DTC but that in the case of *vab-3* loss of function (Meighan and Schwarzbauer, 2007), GON-1 secretion continues in adulthood to cause perpetual gonad elongation. Also, we speculate that the absence of perpetual elongation of the tumorous germline of *glp-1* gain-of-function mutants, such as *glp-1(ar202)* (Pepper et al., 2003) and *gld-1;gld-2* mutants (Kadyk and Kimble, 1998), can be explained in two ways. (1) The absence of ectopic metalloproteases secretion at the DTC tip in these mutants and (2) because the tumor in these worms arises due to a failure to enter meiosis rather than by promoting mitosis directly, meaning that the increase in the number of germ cells in the adult tumorous germline is balanced out by the absence of four-times-larger oocytes, such that the overall pressure within the gonad remains similar between wild-type and tumorous gonads. Hence, overextended gonadal arms have not been observed in tumor mutants (Kadyk and Kimble, 1998; Pepper et al., 2003).

Key regulators of gonad turning include netrin signaling, Src kinases, and several cell-matrix adhesion related proteins (Baum and Garriga, 1997; Chan et al., 1996; Cram et al., 2003; Hedgecock et al., 1990; Lee et al., 2001a; Leung-Hagesteijn et al., 1992; Meighan and Schwarzbauer, 2014, 2007; Su et al., 2000; Wong et al., 2014). Although it has been established that each of these components play a role in DTC reorientation, the relationship between them and the mechanics of turning were unknown. We developed a qualitative theoretical model to explain gonad turning, which has not been addressed by any of the previous mathematical models of the *C. elegans* germline (Atwell et al., 2015; Chiang et al., 2015; Hall et al., 2015). Based on our physical model, we predicted that an asymmetric, localized accumulation of cell-matrix adhesion proteins, which act as an axis or ''hinge point,'' concurrent with a proliferative pushing force behind the DTC, would result in a net torque. In response to this torque, the DTC rotates about the hinge point resulting in gonad turning (Figure 5). In contrast with the literature that proposes two separate turns (Hedgecock et al., 1987; Nishiwaki, 1999), our model proposes that gonad folding takes place through a single U-turn. Weaker adhesion during the turn leads to an ''S-shaped'' gonad morphology, while stronger adhesion results in ''snail-shaped'' gonads. Three experimental observations support our predicted model. First, polarized enrichment of integrins (PAT-3 and INA-1) and Talin (TLN-1) in the dorsal turn (Figure 5). Second, DTC-specific depletion of PAT-3, INA-1, and TLN-1 resulted in S-shaped gonads, while the upregulation of INA-1 via *vab-3* (RNAi) resulted in a snail-shaped morphology (Figure 6). Third, reversal of integrin polarity in the ventralized turn of *unc-5* mutants. During gonad elongation on the dorsal and ventral surface, adhesions are distributed uniformly around the DTC (Figure 7).

We found that the polarized distribution of adhesion is regulated by CDC-42 and SRC-1. In the absence of CDC-42 and SRC-1, gonads either fail to turn or turn in the wrong direction. We speculate that the phenotype of complete failure to turn, which is stronger than the S-shaped phenotype observed with single-integrin depletion, is due to regulation of more than one of the integrins by CDC-42 and SRC-1 (Figure 7). Whether CDC-42 and SRC-1 regulate adhesion proteins directly or indirectly merits further investigation. Thus, seamless turning of the gonad requires a navigation chemotactic signal, i.e., netrin signaling, as reported previously (Chan et al., 1996; Hedgecock et al., 1990; Leung-Hagesteijn et al., 1992), and a spatially regulated cell-matrix anchorage. In an analogous situation, chemotaxis and durotaxis collectively drive efficient neural crest cell migration in *Xenopus* (Shellard and Mayor, 2021). Broadly, it reveals that molecular cues coordinate with mechanics to drive organogenesis in different systems.

In summary, we propose that gonad morphogenesis results from the combined action of germ cells confined in a basement membrane and the DTC cap. Although the proliferation of germ cells provides the driving force that propels the motion of the DTC, the DTC steers the motion by secreting metalloproteases and by selectively forming cell-matrix adhesions in the direction of the turn.

Limitations of the study

We observed that the DTC is polarized with NMY-2 enriched at the rear and ARX-2 puncta at the front of the DTC (Figure 1E). However, we do not understand the significance of this polarity. Our study demonstrates that proliferative pressure provides the pushing force for DTC invasion and tissue elongation, yet the quantitative measurement of pressure within the gonad warrants technical advancement in the future (Figures 2 and 3). We observed that loss of GLP-1, a germ cell-specific Notch receptor, affects DTC morphology (Figure 3E), but the reason for it is unclear. Also, it is unknown what regulates the localization of GON-1 metalloprotease, specifically at the DTC tip during different stages of gonad development (Figure 4B). DTC has polarized localization of cell-matrix adhesion receptors during the turn, but after the turn adhesion receptors are symmetrically distributed (Figure 5). How a polarized DTC switches to an unpolarized cell needs to be further explored.

STAR★METHODS

Detailed methods are provided in the online version of this paper and include the following:

- KEY RESOURCES TABLE
- RESOURCE AVAILABILITY
  - Lead contact
  - Materials availability
  - Data and code availability
- EXPERIMENTAL MODEL DETAILS
  - Worm strain maintenance
- METHOD DETAILS
  - RNA interference
  - Phalloidin staining
  - Imaging and laser ablation
  - FRAP (Fluorescence Recovery after Photobleaching)
  - Quantification of gonad and DTC morphometrics
  - Fluorescent intensity measurement
  - Extended theory
- QUANTIFICATION AND STATISTICAL ANALYSIS

SUPPLEMENTAL INFORMATION

Supplemental information can be found online at https://doi.org/10.1016/j.devcel.2022.08.003.

ACKNOWLEDGMENTS

We thank Dr. Anat Nitzan for generating strain RZB350. This work was supported by Israel Science Foundation grants 767/20 and 3308/20, and funding from the U.S.-Israel Binational Science Foundation grant 2021014 awarded to R.Z.-B., and Israel Science Foundation grant 2751/20 awarded to T.S.

AUTHOR CONTRIBUTIONS

P.A. conceptualized the project, performed all experiments, analyzed and visualized data, and wrote the paper; T.S. contributed conceptualization, performed physical modeling, and contributed to the writing of the paper; R.Z.-B. contributed conceptualization, obtained funding, analyzed data, and wrote the paper.

DECLARATION OF INTERESTS

The authors declare no competing interests.

Received: May 4, 2022
Revised: July 3, 2022
Accepted: August 9, 2022
Published: August 31, 2022

REFERENCES

Abrams, J., and Nance, J. (2021). A polarity pathway for exocyst-dependent intracellular tube extension. eLife. *10*, e65169. https://doi.org/10.7554/eLife.65169.

Agarwal, P., and Zaidel-Bar, R. (2019). Diverse roles of non-muscle myosin II contractility in 3D cell migration. Essays Biochem. *63*, 497–508. https://doi.org/10.1042/EBC20190026.

Agarwal, P., and Zaidel-Bar, R. (2021). Mechanosensing in embryogenesis. Curr. Opin. Cell Biol. *68*, 1–9. https://doi.org/10.1016/j.ceb.2020.08.007.

Andrew, D.J., and Ewald, A.J. (2010). Morphogenesis of epithelial tubes: insights into tube formation, elongation, and elaboration. Dev. Biol. *341*, 34–55. https://doi.org/10.1016/j.ydbio.2009.09.024.

Aratyn-Schaus, Y., and Gardel, M.L. (2010). Transient frictional slip between integrin and the ECM in focal adhesions under myosin II tension. Curr. Biol. *20*, 1145–1153. https://doi.org/10.1016/j.cub.2010.05.049.

Atwell, K., Qin, Z., Gavaghan, D., Kugler, H., Hubbard, E.J.A., and Osborne, J.M. (2015). Mechano-logical model of C. elegans germ line suggests feedback on the cell cycle. Development *142*, 3902–3911. https://doi.org/10.1242/dev.126359.

Backholm, M., Ryu, W.S., and Dalnoki-Veress, K. (2013). Viscoelastic properties of the nematode Caenorhabditis elegans, a self-similar, shear-thinning worm. Proc. Natl. Acad. Sci. USA *110*, 4528–4533. https://doi.org/10.1073/pnas.1219965110.

Baum, P.D., and Garriga, G. (1997). Neuronal migrations and axon fasciculation are disrupted in ina-1 integrin mutants. Neuron *19*, 51–62. https://doi.org/10.1016/s0896-6273(00)80347-5.

Berger, S., Lattmann, E., Aegerter-Wilmsen, T., Hengartner, M., Hajnal, A., DeMello, A., and Casadevall i Solvas, X. (2018). Long-term C. elegans immobilization enables high resolution developmental studies in vivo. Lab Chip *18*, 1359–1368. https://doi.org/10.1039/c7lc01185g.

Blanchoin, L., Boujemaa-Paterski, R., Sykes, C., and Plastino, J. (2014). Actin dynamics, architecture, and mechanics in cell motility. Physiol. Rev. *94*, 235–263. https://doi.org/10.1152/physrev.00018.2013.

Blelloch, R., Anna-Arriola, S.S., Gao, D., Li, Y., Hodgkin, J., and Kimble, J. (1999). The gon-1 gene is required for gonadal morphogenesis in *Caenorhabditis elegans*. Dev. Biol. *216*, 382–393. https://doi.org/10.1006/dbio.1999.9491.

Blelloch, R., and Kimble, J. (1999). Control of organ shape by a secreted metalloprotease in the nematode *Caenorhabditis elegans*. Nature *399*, 586–590. https://doi.org/10.1038/21196.

Bonnet, I., Marcq, P., Bosveld, F., Fetler, L., Bellaïche, Y., and Graner, F. (2012). Mechanical state, material properties and continuous description of an epithelial tissue. J. R. Soc. Interface *9*, 2614–2623. https://doi.org/10.1098/rsif.2012.0263.

Brakke, K.A. (1992). The surface evolver. Exp. Math. *1*, 141–165. https://doi.org/10.1080/10586458.1992.10504253.

Brenner, S. (1974). The genetics of *Caenorhabditis elegans*. Genetics *77*, 71–94. https://doi.org/10.1093/genetics/77.1.71.

Cecchetelli, A.D., and Cram, E.J. (2017). Regulating distal tip cell migration in space and time. Mech. Dev. *148*, 11–17. https://doi.org/10.1016/j.mod.2017.04.003.

Chan, C.E., and Odde, D.J. (2008). Traction dynamics of filopodia on compliant substrates. Science *322*, 1687–1691. https://doi.org/10.1126/science.1163595.

Chan, S.S.Y., Zheng, H., Su, M.W., Wilk, R., Killeen, M.T., Hedgecock, E.M., and Culotti, J.G. (1996). UNC-40, a *C. elegans* homolog of DCC (deleted in colorectal cancer), is required in motile cells responding to UNC-6 netrin cues. Cell *87*, 187–195. https://doi.org/10.1016/s0092-8674(00)81337-9.

Chaudhuri, O., Cooper-White, J., Janmey, P.A., Mooney, D.J., and Shenoy, V.B. (2020). Effects of extracellular matrix viscoelasticity on cellular behaviour. Nature *584*, 535–546. https://doi.org/10.1038/s41586-020-2612-2.

Chiang, M., Cinquin, A., Paz, A., Meeds, E., Price, C.A., Welling, M., and Cinquin, O. (2015). Control of *Caenorhabditis elegans* germ-line stem-cell cycling speed meets requirements of design to minimize mutation accumulation. BMC Biol. *13*, 51. https://doi.org/10.1186/s12915-015-0148-y.

Cram, E.J., Clark, S.G., and Schwarzbauer, J.E. (2003). Talin loss-of-function uncovers roles in cell contractility and migration in *C. elegans*. J. Cell Sci. *116*, 3871–3878. https://doi.org/10.1242/jcs.00705.

Cram, E.J., Shang, H., and Schwarzbauer, J.E. (2006). A systematic RNA interference screen reveals a cell migration gene network in *C. elegans*. J. Cell Sci. *119*, 4811–4818. https://doi.org/10.1242/jcs.03274.

Crest, J., Diz-Muñoz, A., Chen, D.-Y., Fletcher, D.A., and Bilder, D. (2017). Organ sculpting by patterned extracellular matrix stiffness. eLife *6*, e24958. https://doi.org/10.7554/eLife.24958.

Critchley, D.R. (2005). Genetic, biochemical and structural approaches to talin function. Biochem. Soc. Trans. *33*, 1308–1312. https://doi.org/10.1042/BST20051308.

Crittenden, S.L., Leonhard, K.A., Byrd, D.T., and Kimble, J. (2006). Cellular analyses of the mitotic region in the *Caenorhabditis elegans* adult germ line. Mol. Biol. Cell *17*, 3051–3061. https://doi.org/10.1091/mbc.e06-03-0170.

Etienne-Manneville, S. (2004). Cdc42 - the centre of polarity. J. Cell Sci. *117*, 1291–1300. https://doi.org/10.1242/jcs.01115.

Etienne-Manneville, S. (2008). Polarity proteins in migration and invasion. Oncogene *27*, 6970–6980. https://doi.org/10.1038/onc.2008.347.

Gaggioli, C., Hooper, S., Hidalgo-Carcedo, C., Grosse, R., Marshall, J.F., Harrington, K., and Sahai, E. (2007). Fibroblast-led collective invasion of carcinoma cells with differing roles for RhoGTPases in leading and following cells. Nat. Cell Biol. *9*, 1392–1400. https://doi.org/10.1038/ncb1658.

Gettner, S.N., Kenyon, C., and Reichardt, L.F. (1995). Characterization of beta pat-3 heterodimers, a family of essential integrin receptors in *C. elegans*. J. Cell Biol. *129*, 1127–1141. https://doi.org/10.1083/jcb.129.4.1127.

Gibson, D.G., Young, L., Chuang, R.-Y., Venter, J.C., Hutchison, C.A., and Smith, H.O. (2009). Enzymatic assembly of DNA molecules up to several hundred kilobases. Nat. Methods *6*, 343–345. https://doi.org/10.1038/nmeth.1318.

Gilmour, D., Rembold, M., and Leptin, M. (2017). From morphogen to morphogenesis and back. Nature *541*, 311–320. https://doi.org/10.1038/nature21348.

Gilpin, W., Uppaluri, S., and Brangwynne, C.P. (2015). Worms under pressure: bulk mechanical properties of *C. elegans* are independent of the cuticle. Biophys. J. *108*, 1887–1898. https://doi.org/10.1016/j.bpj.2015.03.020.

Gordon, K.L., Zussman, J.W., Li, X., Miller, C., and Sherwood, D.R. (2020). Stem cell niche exit in *C. elegans* via orientation and segregation of daughter cells by a cryptic cell outside the niche. eLife *9*, 1–56. https://doi.org/10.7554/eLife.56383.

Gotta, M., Abraham, M.C., and Ahringer, J. (2001). CDC-42 controls early cell polarity and spindle orientation in *C. elegans*. Curr. Biol. *11*, 482–488. https://doi.org/10.1016/S0960-9822(01)00142-7.

Hall, B.A., Piterman, N., Hajnal, A., and Fisher, J. (2015). Emergent stem cell homeostasis in the *C. elegans* germline is revealed by hybrid modeling. Biophys. J. *109*, 428–438. https://doi.org/10.1016/j.bpj.2015.06.007.

Hall, D.H., Winfrey, V.P., Blaeuer, G., Hoffman, L.H., Furuta, T., Rose, K.L., Hobert, O., and Greenstein, D. (1999). Ultrastructural features of the adult hermaphrodite gonad of *Caenorhabditis elegans*: relations between the germ line and soma. Dev. Biol. *212*, 101–123. https://doi.org/10.1006/dbio.1999.9356.

Harunaga, J.S., Doyle, A.D., and Yamada, K.M. (2014). Local and global dynamics of the basement membrane during branching morphogenesis require protease activity and actomyosin contractility. Dev. Biol. *394*, 197–205. https://doi.org/10.1016/j.ydbio.2014.08.014.

Hedgecock, E.M., Culotti, J.G., and Hall, D.H. (1990). The unc-5, unc-6, and unc-40 genes guide circumferential migrations of pioneer axons and mesodermal cells on the epidermis in *C. elegans*. Neuron *4*, 61–85. https://doi.org/10.1016/0896-6273(90)90444-K.

Hedgecock, E.M., Culotti, J.G., Hall, D.H., and Stern, B.D. (1987). Genetics of cell and axon migrations in *Caenorhabditis elegans*. Development *100*, 365–382. https://doi.org/10.1242/dev.100.3.365.

Heppert, J.K., Dickinson, D.J., Pani, A.M., Higgins, C.D., Steward, A., Ahringer, J., Kuhn, J.R., and Goldstein, B. (2016). Comparative assessment of fluorescent proteins for in vivo imaging in an animal model system. Mol. Biol. Cell *27*, 3385–3394. https://doi.org/10.1091/mbc.E16-01-0063.

Huang, C.-C., Hall, D.H., Hedgecock, E.M., Kao, G., Karantza, V., Vogel, B.E., Hutter, H., Chisholm, A.D., Yurchenco, P.D., and Wadsworth, W.G. (2003). Laminin alpha subunits and their role in *C. elegans* development. Development *130*, 3343–3358. https://doi.org/10.1242/dev.00481.

Ihara, S., Hagedorn, E.J., Morrissey, M.A., Chi, Q., Motegi, F., Kramer, J.M., and Sherwood, D.R. (2011). Basement membrane sliding and targeted adhesion remodels tissue boundaries during uterine–vulval attachment in *Caenorhabditis elegans*. Nat. Cell Biol. *13*, 641–651. https://doi.org/10.1038/ncb2233.

Itoh, B., Hirose, T., Takata, N., Nishiwaki, K., Koga, M., Ohshima, Y., and Okada, M. (2005). SRC-1, a non-receptor type of protein tyrosine kinase, controls the direction of cell and growth cone migration in *C. elegans*. Development *132*, 5161–5172. https://doi.org/10.1242/dev.02103.

Kadyk, L.C., and Kimble, J. (1998). Genetic regulation of entry into meiosis in *Caenorhabditis elegans*. Development *125*, 1803–1813. https://doi.org/10.1242/dev.125.10.1803.

Kamath, R.S., and Ahringer, J. (2003). Genome-wide RNAi screening in *Caenorhabditis elegans*. Methods *30*, 313–321. https://doi.org/10.1016/S1046-2023(03)00050-1.

Kay, A.J., and Hunter, C.P. (2001). CDC-42 regulates PAR protein localization and function to control cellular and embryonic polarity in *C. elegans*. Curr. Biol. *11*, 474–481. https://doi.org/10.1016/S0960-9822(01)00141-5.

Keeley, D.P., Hastie, E., Jayadev, R., Kelley, L.C., Chi, Q., Payne, S.G., Jeger, J.L., Hoffman, B.D., and Sherwood, D.R. (2020). Comprehensive endogenous tagging of basement membrane components reveals dynamic movement within the matrix scaffolding. Dev. Cell *54*, 60–74.e7. https://doi.org/10.1016/j.devcel.2020.05.022.

Kershner, A.M., Shin, H., Hansen, T.J., and Kimble, J. (2014). Discovery of two GLP-1/Notch target genes that account for the role of GLP-1/Notch signaling in stem cell maintenance. Proc. Natl. Acad. Sci. USA *111*, 3739–3744. https://doi.org/10.1073/pnas.1401861111.

Khalilgharibi, N., Fouchard, J., Asadipour, N., Barrientos, R., Duda, M., Bonfanti, A., Yonis, A., Harris, A., Mosaffa, P., Fujita, Y., et al. (2019). Stress relaxation in epithelial monolayers is controlled by the actomyosin cortex. Nat. Phys. *15*, 839–847. https://doi.org/10.1038/s41567-019-0516-6.

Killian, D.J., and Hubbard, E.J.A. (2005). *Caenorhabditis elegans* germline patterning requires coordinated development of the somatic gonadal sheath and the germ line. Dev. Biol. *279*, 322–335. https://doi.org/10.1016/j.ydbio.2004.12.021.

Kimble, J., and Crittenden, S.L. (2005). Germline proliferation and its control. WormBook *1–14*, 1–14. https://doi.org/10.1895/wormbook.1.13.1.

Kimble, J.E., and White, J.G. (1981). On the control of germ cell development in Caenorhabditis elegans. Dev. Biol. *81*, 208–219. https://doi.org/10.1016/0012-1606(81)90284-0.

Kodoyianni, V., Maine, E.M., and Kimble, J. (1992). Molecular basis of loss-of-function mutations in the glp-1 gene of *Caenorhabditis elegans*. Mol. Biol. Cell *3*, 1199–1213. https://doi.org/10.1091/mbc.3.11.1199.

Kyprianou, C., Christodoulou, N., Hamilton, R.S., Nahaboo, W., Boomgaard, D.S., Amadei, G., Migeotte, I., and Zernicka-Goetz, M. (2020). Basement membrane remodelling regulates mouse embryogenesis. Nature *582*, 253–258. https://doi.org/10.1038/s41586-020-2264-2.

Lee, J., Li, W., and Guan, K.-L. (2005). SRC-1 mediates UNC-5 signaling in Caenorhabditis elegans. Mol. Cell. Biol. *25*, 6485–6495. https://doi.org/10.1128/MCB.25.15.6485-6495.2005.

Lee, M., Cram, E.J., Shen, B., and Schwarzbauer, J.E. (2001a). Roles for βpat-3 integrins in development and function of *Caenorhabditis elegans* muscles and gonads. J. Biol. Chem. *276*, 36404–36410. https://doi.org/10.1074/jbc.M105795200.

Leung-Hagesteijn, C., Spence, A.M., Stern, B.D., Zhou, Y., Su, M.W., Hedgecock, E.M., and Culotti, J.G. (1992). UNC-5, a transmembrane protein with immunoglobulin and thrombospondin type 1 domains, guides cell and pioneer axon migrations in *C. elegans*. Cell *71*, 289–299. https://doi.org/10.1016/0092-8674(92)90357-I.

Linden, L.M., Gordon, K.L., Pani, A.M., Payne, S.G., Garde, A., Burkholder, D., Chi, Q., Goldstein, B., and Sherwood, D.R. (2017). Identification of regulators of germ stem cell enwrapment by its niche in *C. elegans*. Dev. Biol. *429*, 271–284. https://doi.org/10.1016/j.ydbio.2017.06.019.

Llamazares, M., Cal, S., Quesada, V., and López-Otín, C. (2003). Identification and characterization of ADAMTS-20 defines a novel subfamily of metalloproteinases-disintegrins with multiple thrombospondin-1 repeats and a unique GON domain. J. Biol. Chem. *278*, 13382–13389. https://doi.org/10.1074/jbc.M211900200.

Marston, D.J., Higgins, C.D., Peters, K.A., Cupp, T.D., Dickinson, D.J., Pani, A.M., Moore, R.P., Cox, A.H., Kiehart, D.P., and Goldstein, B. (2016). MRCK-1 drives apical constriction in *C. elegans* by linking developmental patterning to force generation. Curr. Biol. *26*, 2079–2089. https://doi.org/10.1016/j.cub.2016.06.010.

Meighan, C.M., and Schwarzbauer, J.E. (2007). Control of *C. elegans* hermaphrodite gonad size and shape by vab-3/Pax6-mediated regulation of integrin receptors. Genes Dev. *21*, 1615–1620. https://doi.org/10.1101/gad.1534807.

Meighan, C.M., and Schwarzbauer, J.E. (2014). α integrin cytoplasmic tails have tissue-specific roles during *C. elegans* development. Int. J. Dev. Biol. *58*, 325–333. https://doi.org/10.1387/ijdb.130327cm.

Mongera, A., Rowghanian, P., Gustafson, H.J., Shelton, E., Kealhofer, D.A., Carn, E.K., Serwane, F., Lucio, A.A., Giammona, J., and Campàs, O. (2018). A fluid-to-solid jamming transition underlies vertebrate body axis elongation. Nature *561*, 401–405. https://doi.org/10.1038/s41586-018-0479-2.

Moulder, G.L., Huang, M.M., Waterston, R.H., and Barstead, R.J. (1996). Talin requires beta-integrin, but not vinculin, for its assembly into focal adhesion-like structures in the nematode *Caenorhabditis elegans*. Mol. Biol. Cell *7*, 1181–1193. https://doi.org/10.1091/mbc.7.8.1181.

Munjal, A., Hannezo, E., Tsai, T.Y.C., Mitchison, T.J., and Megason, S.G. (2021). Extracellular hyaluronate pressure shaped by cellular tethers drives tissue morphogenesis. Cell *184*, 6313–6325.e18. https://doi.org/10.1016/j.cell.2021.11.025.

Nishiwaki, K. (1999). Mutations affecting symmetrical migration of distal tip cells in *Caenorhabditis elegans*. Genetics *152*, 985–997. https://doi.org/10.1093/genetics/152.3.985.

Nishiwaki, K., Hisamoto, N., and Matsumoto, K. (2000). A metalloprotease disintegrin that controls cell migration in *Caenorhabditis elegans*. Science *288*, 2205–2208. https://doi.org/10.1126/science.288.5474.2205.

Pazdernik, N., and Schedl, T. (2013). Introduction to germ cell development in *Caenorhabditis elegans*. Adv. Exp. Med. Biol. *757*, 1–16. https://doi.org/10.1007/978-1-4614-4015-4_1.

Pepper, A.S.R., Lo, T.W., Killian, D.J., Hall, D.H., and Hubbard, E.J.A. (2003). The establishment of *Caenorhabditis elegans* germline pattern is controlled by overlapping proximal and distal somatic gonad signals. Dev. Biol. *259*, 336–350. https://doi.org/10.1016/s0012-1606(03)00203-3.

Petridou, N.I., Spiró, Z., and Heisenberg, C.-P. (2017). Multiscale force sensing in development. Nat. Cell Biol. *19*, 581–588. https://doi.org/10.1038/ncb3524.

Phair, R.D., Gorski, S.A., and Misteli, T. (2004). Measurement of dynamic protein binding to chromatin in vivo, using photobleaching microscopy. Methods Enzymol. *375*, 393–414. https://doi.org/10.1016/S0076-6879(03)75025-3.

Pichaud, F., Walther, R.F., and Nunes de Almeida, F. (2019). Regulation of Cdc42 and its effectors in epithelial morphogenesis. J. Cell Sci. *132*, jcs217869. https://doi.org/10.1242/jcs.217869.

Playford, M.P., and Schaller, M.D. (2004). The interplay between Src and integrins in normal and tumor biology. Oncogene *23*, 7928–7946. https://doi.org/10.1038/sj.onc.1208080.

Priti, A., Ong, H.T., Toyama, Y., Padmanabhan, A., Dasgupta, S., Krajnc, M., and Zaidel-Bar, R. (2018). Syncytial germline architecture is actively maintained by contraction of an internal actomyosin corset. Nat. Commun. *9*, 4694. https://doi.org/10.1038/s41467-018-07149-2.

Rappel, W.-J., and Edelstein-Keshet, L. (2017). Mechanisms of cell polarization. Curr. Opin. Syst. Biol. *3*, 43–53. https://doi.org/10.1016/j.coisb.2017.03.005.

Reddien, P.W., and Horvitz, H.R. (2000). CED-2/CrkII and CED-10/Rac control phagocytosis and cell migration in *Caenorhabditis elegans*. Nat. Cell Biol. *2*, 131–136. https://doi.org/10.1038/35004000.

Ridley, A.J., Schwartz, M.A., Burridge, K., Firtel, R.A., Ginsberg, M.H., Borisy, G., Parsons, J.T., and Horwitz, A.R. (2003). Cell migration: integrating signals from front to back. Science *302*, 1704–1709. https://doi.org/10.1126/science.1092053.

Rohrschneider, M.R., and Nance, J. (2009). Polarity and cell fate specification in the control of *Caenorhabditis elegans* gastrulation. Dev. Dyn. *238*, 789–796. https://doi.org/10.1002/dvdy.21893.

Schindelin, J., Arganda-Carreras, I., Frise, E., Kaynig, V., Longair, M., Pietzsch, T., Preibisch, S., Rueden, C., Saalfeld, S., Schmid, B., et al. (2012). Fiji: an open-source platform for biological-image analysis. Nat. Methods *9*, 676–682. https://doi.org/10.1038/nmeth.2019.

Shattil, S.J., Kim, C., and Ginsberg, M.H. (2010). The final steps of integrin activation: the end game. Nat. Rev. Mol. Cell Biol. *11*, 288–300. https://doi.org/10.1038/nrm2871.

Shellard, A., and Mayor, R. (2021). Collective durotaxis along a self-generated stiffness gradient in vivo. Nature *600*, 690–694. https://doi.org/10.1038/s41586-021-04210-x.

Shemesh, T., Bershadsky, A.D., and Kozlov, M.M. (2012). Physical model for self-organization of actin cytoskeleton and adhesion complexes at the cell front. Biophys. J. *102*, 1746–1756. https://doi.org/10.1016/J.BPJ.2012.03.006.

Sherwood, D.R., and Plastino, J. (2018). Invading, leading and navigating cells in *Caenorhabditis elegans*: insights into cell movement in vivo. Genetics *208*, 53–78. https://doi.org/10.1534/genetics.117.300082.

Simmer, F., Moorman, C., van der Linden, A.M., Kuijk, E., van den Berghe, P.V.E., Kamath, R.S., Fraser, A.G., Ahringer, J., and Plasterk, R.H.A. (2003). Genome-wide RNAi of *C. elegans* using the hypersensitive rrf-3 strain reveals novel gene functions. PLoS Biol. *1*, E12. https://doi.org/10.1371/journal.pbio.0000012.

Somerville, R.P.T., Longpre, J.-M., Jungers, K.A., Engle, J.M., Ross, M., Evanko, S., Wight, T.N., Leduc, R., and Apte, S.S. (2003). Characterization of ADAMTS-9 and ADAMTS-20 as a distinct ADAMTS subfamily related to *Caenorhabditis elegans* gon-1. J. Biol. Chem. *278*, 9503–9513. https://doi.org/10.1074/jbc.M211009200.

Sprague, B.L., Pego, R.L., Stavreva, D.A., and McNally, J.G. (2004). Analysis of binding reactions by fluorescence recovery after photobleaching. Biophys. J. *86*, 3473–3495. https://doi.org/10.1529/biophysj.103.026765.

Sturm, Á., Saskoï, É., Tibor, K., Weinhardt, N., and Vellai, T. (2018). Highly efficient RNAi and Cas9-based auto-cloning systems for *C. elegans* research. Nucleic Acids Res. *46*, e105. https://doi.org/10.1093/NAR/GKY516.

Su, M., Merz, D.C., Killeen, M.T., Zhou, Y., Zheng, H., Kramer, J.M., Hedgecock, E.M., and Culotti, J.G. (2000). Regulation of the UNC-5 netrin receptor initiates the first reorientation of migrating distal tip cells in *Caenorhabditis elegans*. Development *127*, 585–594. https://doi.org/10.1242/dev.127.3.585.

Tannoury, H., Rodriguez, V., Kovacevic, I., Ibourk, M., Lee, M., and Cram, E.J. (2010). CACN-1/Cactin interacts genetically with MIG-2 GTPase signaling to control distal tip cell migration in *C. elegans*. Dev. Biol. *341*, 176–185. https://doi.org/10.1016/j.ydbio.2010.02.025.

Tetley, R.J., and Mao, Y. (2018). The same but different: cell intercalation as a driver of tissue deformation and fluidity. Philos. Trans. R. Soc. Lond. B Biol. Sci. *373*, 20170328. https://doi.org/10.1098/rstb.2017.0328.

Timmons, L. (2006). Delivery methods for RNA interference in *C. elegans*. Methods Mol. Biol. *351*, 119–125. https://doi.org/10.1385/1-59745-151-7:119.

Walck-Shannon, E., and Hardin, J. (2014). Cell intercalation from top to bottom. Nat. Rev. Mol. Cell Biol. *15*, 34–48. https://doi.org/10.1038/nrm3723.

Walser, M., Umbricht, C.A., Fröhli, E., Nanni, P., and Hajnal, A. (2017). β-Integrin de-phosphorylation by the density-enhanced phosphatase DEP-1 attenuates EGFR signaling in *C. elegans*. PLoS Genet. *13*, e1006592. https://doi.org/10.1371/journal.pgen.1006592.

Wolke, U., Jezuit, E.A., and Priess, J.R. (2007). Actin-dependent cytoplasmic streaming in *C. elegans* oogenesis. Development *134*, 2227–2236. https://doi.org/10.1242/dev.004952.

Wong, M.-C., Kennedy, W.P., and Schwarzbauer, J.E. (2014). Transcriptionally regulated cell adhesion network dictates distal tip cell directionality. Dev. Dyn. *243*, 999–1010. https://doi.org/10.1002/dvdy.24146.

Wong, M.-C., and Schwarzbauer, J.E. (2012). Gonad morphogenesis and distal tip cell migration in the *Caenorhabditis elegans* hermaphrodite. Wiley Interdiscip. Rev. Dev. Biol. *1*, 519–531. https://doi.org/10.1002/wdev.45.

Zacharias, A.L., Walton, T., Preston, E., and Murray, J.I. (2015). Quantitative differences in nuclear β-catenin and TCF pattern embryonic cells in *C. elegans*. PLoS Genet. *11*, e1005585. https://doi.org/10.1371/journal.pgen.1005585.

Zhang, Y., Yang, Y., Zhu, Z., and Ou, G. (2017). WASP-Arp2/3-dependent actin polymerization influences fusogen localization during cell-cell fusion in *Caenorhabditis elegans* embryos. Biol. Open *6*, 1324–1328. https://doi.org/10.1242/bio.026807.

Zhu, Z., Chai, Y., Jiang, Y., Li, W., Hu, H., Li, W., Wu, J.-W., Wang, Z.-X., Huang, S., and Ou, G. (2016). Functional coordination of WAVE and WASP in C. elegans neuroblast migration. Dev. Cell *39*, 224–238. https://doi.org/10.1016/j.devcel.2016.09.029.

Please cite this article in press as: Agarwal et al., Directed cell invasion and asymmetric adhesion drive tissue elongation and turning in *C. elegans* gonad morphogenesis, Developmental Cell (2022), https://doi.org/10.1016/j.devcel.2022.08.003

STAR★METHODS

KEY RESOURCES TABLE

REAGENT or RESOURCE	SOURCE	IDENTIFIER
Experimental models: Organisms/strains		
cpIs121 I; rrf-3(pk1426) II; rde-1(ne219) V.	Linden et al., 2017	NK2115
cpIs121 I; rrf-3(pk1426) II; rde-1(ne219) V;ltIs44 [Ppie-1::mCherry::PH(PLC1delta1); unc-119(+)] IV	This study	RZB353
nmy-2(cp52 [nmy-2::kate + LoxP unc-119 (+) Lox P]) I; unc-119 (ed3) III	Heppert et al., 2016	LP229
mig-24p::LifeAct::WrmScarlet	This study	RZB421
cpIs121 I; rrf-3(pk1426) II; rde-1(ne219) V;tba-1 ((knu639 [pNU1541 - N-terminal degron mKate2 unc-119(+)] unc-119(ed3) III))I	This study	RZB354
cas607[arx-2::gfp knock-in] V)	Zhu et al., 2016	GOU2047
cas723 [gfp::wsp-1 knock-in]	Zhu et al., 2016	GOU2049
cas728 [gfp::wve-1 knock-in]	Zhu et al., 2016	GOU2050
cas725 [arx-2::TagRFP knock-in]	Zhang et al., 2017	GOU2905
cyk-1 (knu83 C-terminal GFP, unc-119 (+)); unc-119(ed3) III	Priti et al., 2018	COP942
rrf-3(pk1426) II; nmy-2 (cp52[nmy-2::mkate]) I; cas607[arx-2::gfp knock-in] V	This study	RZB368
unc-119(ed4) III; qyIs108.	Ihara et al., 2011	NK651
ujIs113 [pie-1p::mCherry::H2B::pie-1 3'UTR + nhr-2p::his-24::mCherry::let-858 3'UTR + unc-119(+)]	Zacharias et al., 2015	JIM113
unc-119(ed4) III; qyIs108; ujIs113 [pie-1p::mCherry::H2B::pie-1 3'UTR + nhr-2p::his-24::mCherry::let-858 3'UTR + unc-119(+)]	This study	RZB367
glp-1(bn18) III	Kodoyianni et al., 1992	DG2389
glp-1(bn18) I; unc-119(ed4) III; qyIs108; ujIs113 [pie-1p::mCherry::H2B::pie-1 3'UTR + nhr-2p::his-24::mCherry::let-858 3'UTR + unc-119(+)]	This study	RZB377
pat-3(zh115[gfp::pat-3]) I.	Gift from Alex Hajnal, University of Zurich	AH4617
tln-1(zh117[gfp::tln-1]) I.	Walser et al., 2017	AH3437
ina-1(qy23[ina-1::mNG]) III	Keeley et al., 2020	NK2324
gon-1(qy45[gon-1::mNG+loxP]) IV.	Keeley et al., 2020	NK2590
mig-24p::SKI-Lodge casette::WrmScarlet	This study	RZB350
rrf-3(pk1426); pat-3::GFP; mig-24p::SKI-Lodge casette::WrmScarlet	This study	RZB392
glp-1(bn18) III; cpIs121 I	This study	RZB418
mig-24p::SKI-Lodge casette::WrmScarlet; qyIs108 [lam-1p::lam-1::dendra + unc-119(+)]	This study	RZB422
mig-24p::SKI-Lodge casette::WrmScarlet; ina-1(qy23[ina-1::mNG]) III	This study	RZB423

(*Continued on next page*)

Continued

REAGENT or RESOURCE	SOURCE	IDENTIFIER
Oligonucleotides		
Forward primer for nmy-2 with T444T overhangs TCTGATATCATCGATGAA TTCGAGCTCCACTCAGGCTGTTCTG CTCAATG	This study	N/A
Reverse primer for nmy-2 with T444T overhangs CCCTCGAGGTCGACGGT ATCGATAAGCTTGGAGCGAATCTCT GGAACGAC	This study	N/A
Forward primer for vector with overhangs of nmy-2 TCCGAAGTACGTCGTTCCA GAGATTCGCTCCAAGCTTATCGATA CCGTCGAC	This study	N/A
Reverse primer for vector with nmy-2 overhangs GCAACAGCGTCATTGAG CAGAACAGCCTGAGTGGAGCTCGA ATTCATCGATG	This study	N/A
Forward primer for arx-2 with T444T overhangs TCTGATATCATCGATGA ATTCGAGCTCCACTATTCCCTTCAA TGGTCGGTCG	This study	N/A
Reverse primer for arx-2 with T444T overhangs CCCTCGAGGTCGACGG TATCGATAAGCTTGTCGTAAACAGG ACAGATGTGGG	This study	N/A
Forward primer for vector with overhangs of arx-2 TGGTGTTACCCACATCTGTCCT GTTTACGACAAGCTTATCGATACCGTC GAC	This study	N/A
Reverse primer for vector with arx-2 overhangs CGATTGGCCGACCGAC CATTGAAGGGAATAGTGGAGCTCG AATTCATCGATG	This study	N/A
Forward primer for cyk-1 with T444T overhangs TCTGATATCATCGATGA ATTCGAGCTCCACCTTCAGCTCTA CCGCCAATAAC	This study	N/A
Reverse primer for cyk-1 with T444T overhangs CCCTCGAGGTCGACGG TATCGATAAGCTTGCAAGACACCAC CAAGAGTACCA	This study	N/A
Forward primer for vector with overhangs of cyk-1 GCAAATAGTGGTACTCTTGGTG GTGTCTTGCAAGCTTATCGATACCGT CGAC	This study	N/A
Reverse primer for vector with cyk-1 overhangs GACCTCCAGTTATTGGCG GTAGAGCTGAAGGTGGAGCTCGAAT TCATCGATG	This study	N/A
Forward primer for cdc-42 with T444T overhangs TCTGATATCATCGATGAA TTCGAGCTCCACATGCAGACGATCA AGTGCGTC	This study	N/A
Reverse primer for cdc-42 with T444T overhangs CCCTCGAGGTCGACGGT ATCGATAAGCTTGGTCAACGCTGAG CATTCAACGT	This study	N/A

(*Continued on next page*)

Please cite this article in press as: Agarwal et al., Directed cell invasion and asymmetric adhesion drive tissue elongation and turning in *C. elegans* gonad morphogenesis, Developmental Cell (2022), https://doi.org/10.1016/j.devcel.2022.08.003

Continued

REAGENT or RESOURCE	SOURCE	IDENTIFIER
Forward primer for vector with overhangs of cdc-42 AGTGAAATACGTTGAATGCTC AGCGTTGACCAAGCTTATCGATACCG TCGAC	This study	N/A
Reverse primer for vector with cdc-42 overhangs TCCAACGACGACGCACTT GATCGTCTGCATGTGGAGCTCGAAT TCATCGATG	This study	N/A
Forward primer for unc-5 with T444T overhangs TCTGATATCATCGATGA ATTCGAGCTCCACGCGGACTCCTC TCGGATAGTAA	This study	N/A
Reverse for unc-5 with T444T overhangs CCCTCGAGGTCGACGGTATCGATAAG CTTGCTGTTAAGGTGTCCGAAACAGC	This study	N/A
Forward for vector with unc-5 overhangs TTTATCTGGCTGTTTCGGACACCTTAA CAGCAAGCTTATCGATACCGTCGAC	This study	N/A
Reverse for vector with unc-5 overhangs ATCACTGATTACTATCCGAGAGGAGT CCGCGTGGAGCTCGAATTCATCGATG	This study	N/A
Forward primer for src-1 with T444T overhangs TCTGATATCATCGATGAA TTCGAGCTCCACCTGTATGCAGTGT GTACACGTG	This study	N/A
Reverse primer for src-1 with T444T overhangs CCCTCGAGGTCGACGG TATCGATAAGCTTGGATACGGAACC TGTCCCTTTGT	This study	N/A
Forward for vector with src-1 overhangs AGATTATGACAAAGGGACAGGTTCCG TATCCAAGCTTATCGATACCGTCGAC	This study	N/A
Reverse primer for vector with src-1 overhangs TGGTTCTTCACGTGTAC ACACTGCATACAGGTGGAGCTCG AATTCATCGATG	This study	N/A
Software and algorithms		
Metamorph	Molecular devices	7.10.2.240
Fiji	Schindelin et al., 2012	http://fiji.sc/
Excel	Microsoft	Version 16.63.1
GraphPad Prism	GraphPad	Version 9
Imaris	Bitplane	Version 8.4.1
Illustrator	Adobe	Version 2022
Matlab and Surface evolver	Zenodo	https://doi.org/10.5281/zenodo.6778906

RESOURCE AVAILABILITY

Lead contact

Further information and requests for resources and reagents should be directed to and will be fulfilled by the Lead Contact, Ronen Zaidel-Bar (zaidelbar@tauex.tau.ac.il)

Materials availability

All the *C. elegans* strains and resources used in this study will be available upon request with the lead contact.

Data and code availability

- Raw microscopy data reported in this paper will be available upon request with the lead contact

Please cite this article in press as: Agarwal et al., Directed cell invasion and asymmetric adhesion drive tissue elongation and turning in *C. elegans* gonad morphogenesis, Developmental Cell (2022), https://doi.org/10.1016/j.devcel.2022.08.003

- The Matlab and Surface Evolver scripts are available at code & data repository-https://zenodo.org/record/6778907#.YrxOKi0RoWo. Doi is listed in the key resources table.
- Any additional information required to reanalyze the data reported in this paper are available upon request from the lead contact.

EXPERIMENTAL MODEL DETAILS

Worm strain maintenance

Nematode Growth medium (NGM) plates seeded with *E. coli* strain OP50 (Brenner, 1974) were used for growing *C. elegans* strains. All strains were maintained at 20°C, except for the temperature-sensitive strain RZB377, which was maintained at 15°C. To observe the phenotype of loss of GLP-1 function, this strain was shifted at L1 stage to 25°C and imaged at the L4 stage. The genotypes of all strains utilized in this study are detailed in the key resources table.

METHOD DETAILS

RNA interference

RNAi experiments were performed using the feeding method (Timmons, 2006). Worms were fed with HT115 *E. coli* containing the T444T RNAi plasmid (Sturm et al., 2018), which expressed double-stranded RNA for a specific target gene, i.e. *nmy-2*, *arx-2*, *cyk-1*, *cdc-42*, *unc-5*, or *src-1*. T444T RNAi vector is a modified L4440 vector with two additional T7 polymerase terminator sequence at each end of the target gene to prevent the insertion of non-specific vector sequence into the transcribed dsRNA (Sturm et al., 2018). We amplified gene-specific sequences from N2 genomic DNA by PCR and inserted them into the T444T vector using Gibson Assembly (Gibson et al., 2009). Primers used for Gibson Assembly cloning protocol are listed in the key resources table. Transformed HT115 bacteria were grown overnight at 37°C. 1:100 dilution of this overnight culture was again incubated at 37°C with shaking until approximately 0.5 OD was reached and then induced with 1mM IPTG. After 3-4 hours of induction, bacterial culture was seeded on NGM RNAi plates supplemented with 100μg/ml of ampicillin and 1mM IPTG, and let to dry. L1 stage worms were transferred to RNAi plates and fed with the bacteria at 20°C for 48 hours. Knock down of *gon-1*, *pat-3*, *tln-1*, *ina-1* and *vab-3* was performed with bacterial clones obtained from the Ahringer RNAi library (Kamath and Ahringer, 2003). For each experiment, we included RNAi bacteria containing empty T444T or L4440 plasmid as a control. To study the DTC autonomous role, we used DTC-specific RNAi hypersensitive strain (Linden et al., 2017) for the experiments depicted in Figures 1F, 4H, 6B, 6C, 7C, and 7D. To increase the RNAi efficiency in the experiments (Figures 1G–1K), we used RNAi-hypersensitive *rrf-3(pk1426)* (Simmer et al., 2003) background mutation.

Phalloidin staining

For phalloidin staining of the gonads, we followed the protocol described previously (Wolke et al., 2007). In short, gonads were extruded by dissecting L4 stage worms in culture buffer (73mM HEPES pH 6.9, 2mM MgCl2, 5mM KCl, 40mM NaCl, 1.6% sucrose, and 10mM EGTA). Extruded gonads were fixed with 3.5% formaldehyde for 10 minutes and then washed 3 times with 1X PBS. Next, fixed gonads were permeabilized using 0.025% Triton-X100 for 5 minutes. Fixed and permeabilized gonads were stained with Alexa-561 phalloidin (Sigma-Aldrich; 1:250 dilution) and DAPI (Sigma-Aldrich; 1:1000 dilution of 5mg/ml stock) in the dark for 20 minutes. After staining, gonads were washed and mounted with 7ul of vectashield (Vector lab, Cat. No. H-1300) on a 3% agarose pad for fluorescent imaging.

Imaging and laser ablation

For live imaging, 5-10 worms of appropriate stage were anesthetized with 10mM levamisole (5ul) and mounted on a 3% agarose pad placed on a glass slide. For imaging of live, as well as fixed samples, we used a spinning disk confocal (Yokogawa CSU-W1) and a prime 95B sCMOS camera (Photometrics) mounted on a Nikon Ti2E microscope. Images were acquired using 60X or 100X oil-immersion Plan-Apochromat objectives with Z-stack spacing of 0.4 μm or 1μm. Control of image acquisition was done with Metamorph software (Molecular devices, Sunnyvale, California).

For laser ablation we used an iLAS Pulse system (GATACA Systems) with a 355nm laser pulsed at 20Khz with 0.5ns pulse width and an average power of 16mW. Early L4 stage worms expressing lag-2p::PH::GFP, a marker for DTC, were mounted on 3% agarose pads with 10mM levamisole. Single or two simultaneous small line incisions (4-5μm in length) were made on either side of the DTC using 75% laser power with 10 repetitions. Images were acquired at a rate of 1 frame per second for a total duration of 1 minute using a 100X 1.45 NA oil-immersion objective. Displacement of the DTC after the laser ablation was measured using FIJI software (Schindelin et al., 2012). For laser ablations at the loop region of the gonad, a small rectangular ($\sim$ 5 μm X 1 μm) region of interest (ROI) was ablated using 75% laser power with 10 repetition. Images were acquired at a rate of 1 frame per second for a total duration of 37 seconds using a 100X 1.45 NA oil-immersion objective.

FRAP (Fluorescence Recovery after Photobleaching)

We used iLas2 illumination module (GATACA system) fitted on a spinning disk confocal microscope with 100X 1.45 NA oil-immersion objective for our FRAP experiments. Early L4 stage worms expressing laminin::Dendra, a basement membrane component, were

Please cite this article in press as: Agarwal et al., Directed cell invasion and asymmetric adhesion drive tissue elongation and turning in *C. elegans* gonad morphogenesis, Developmental Cell (2022), https://doi.org/10.1016/j.devcel.2022.08.003

mounted on 3% agarose pads with 10mM levamisole. Two small rectangular regions of interest (ROI) ($\sim$ 2 μm X 2 μm) were photobleached simultaneously at the DTC tip and a nearby proximal region of the gonad using 488 nm laser at 80% power for 250ms. Images were acquired at an interval of 30 seconds for a total duration of 8.5 minutes using 50% of 488nm laser power with 400ms exposure time.

Quantification of gonad and DTC morphometrics

The length of the gonad in Figures 2C, 2F, 2H and 4I was determined by measuring the distance between the tip of the DTC and the end of the gonad (marked with arrowhead) using a segmented line tool in FIJI software (Schindelin et al., 2012). For Figures 2C, 2E, and 2H, the total number of germ cells present in 3D in the entire gonad was counted by Spot detection and surface creation tool of Imaris (Oxford Instruments).

In Figure 4I, gonad width was calculated by averaging the width measured at three distinct meiotic regions for each of the gonads for each genotype. Also, the number of germ cells was calculated by averaging the number of germ cells measured at three distinct regions within the gonad (Figure 4I).

Fluorescent intensity measurement

Intensity measurements were performed with FIJI software. Background intensity was quantified from each image at a region outside the worm and subtracted it from the whole image before quantifying the intensity at the region of interest. For the measurement of the intensity of NMY-2::mKate, ARX-2::GFP, CYK-1::GFP in Figures 1I–1K, Laminin-1::Dendra intensity in Figures 4C and 4D, and INA-1::mNG intensity in Figures 6E and 6F, we segmented the DTC using threshold intensity and analyze particle tool of FIJI. Average fluorescent intensity was then measured within this region of interest for each of the fluorescent proteins. For measuring intensity profile as shown in Figures 5B–5G, 7A, 7B, 7E, and 7F, S5, and S6, a 7-pixel wide segmented line was traced along the midplane view of the DTC beginning from the dorsal end till the ventral end (marked as points A and B) and the mean intensity was calculated at each point. The intensity profile graph was plotted using GraphPad Prism 9 software.

For FRAP analysis, average fluorescent intensity of the ROI ($I_{frap}(t)$) was quantified by outlining a 7-pixel thick line at the DTC tip and the proximal region of the gonad before the photo bleach, at the photo bleach time point and subsequent recovery timepoints for 8.5 minutes using FIJI software. We also measured average fluorescent intensity of the background ROI ($I_{BG}(t)$) and unbleached ROI ($I_{UB}(t)$) for each time point. The average fluorescent intensity of the bleached ROI ($I_{frap}(t)$) was corrected for background and photobleaching using the following formula of the double normalization method as described before (Phair et al., 2004):

$$I_{norm}(t) = \frac{I_{UB\_pre}}{I_{UB}(t) - I_{BG}(t)} \cdot \frac{I_{frap}(t) - I_{BG}(t)}{I_{frap\_pre}}$$

The following equation:

$I_{norm\_sc}(t) = \frac{I_{norm}(t) - I_{norm}(t_{bleach})}{I_{norm\_pre} - I_{norm}(t_{bleach})}$ was used for full-scale calibration. t_{bleach} denotes bleach time. The mobile fraction was calculated using single exponential curve fitting function (t)=M(1−e−kt), where M denotes mobile fraction and k represents rate constant (Sprague et al., 2004).

Extended theory

The model system

For the sake of simplicity, we represent the tubular structure of the *C. elegans* gonad as a uniform two-dimensional rectangular contour. One gonad end is assumed to remain fixed, while the remaining end is capped by the DTC cell. In our 2D representation, we model the DTC as a 2D cap attached to the gonad bulk, with cell-matrix adhesions that localize to the front edge of the DTC (Figure 2A). We model DTC-matrix interactions via integrin-based adhesions as elastic discrete springs with an effective spring constant, k. We account for the stick-slip nature of the adhesion mediated friction by resetting the adhesion strain, Δ, when exceeding a critical strain $\Delta > \Delta_c$, where we take $\Delta_c = 0.1\mu m$ (Shemesh et al., 2012).

Model for DTC motion

Proliferation of progenitor cells within the gonad results in an internal pressure that acts to expand its volume. In our model, the internal pressure within the gonad lumen is represented by a 2D pressure acting to expand the area enclosed by the 2D contour. Sheath cells that wrap around the bulk of the gonad provide the required hoop stress to constrain the gonad diameter and are represented in our model by elastic line segments that span the gonad width, constraining it to a diameter D = 20 μm (see Figure S2).

The proliferation of gonad cells results in a net forward pushing force that is applied to the DTC. This pushing force is countered by a reciprocal friction force from the adhesions and drives a forward motion of the DTC. Note that some of the force due to gonad pressure may be additionally countered by longitudinal stress in the gonad's enveloping sheath. Such longitudinal tension effectively lowers the load applied on the adhesions but does not qualitatively affect our model and is therefore not considered here.

Model for DTC turning

Symmetric distribution of cell-matrix adhesions along the DTC periphery results in a net friction force that is parallel to the local orientation of the gonad. On the other hand, an asymmetrical distribution of adhesions will additionally produce a torque that acts to rotate the DTC about the high-adhesion region (see Figure 6A).

Please cite this article in press as: Agarwal et al., Directed cell invasion and asymmetric adhesion drive tissue elongation and turning in *C. elegans* gonad morphogenesis, Developmental Cell (2022), https://doi.org/10.1016/j.devcel.2022.08.003

We model adhesion asymmetry by assigning linearly increasing the adhesions' spring constant, $k(s)$, along the DTC edge: $k(s) = k_0 s/s_{tot}$, where $s = 0$ corresponds to the frontmost tip of the DTC, and $s = 1$ corresponds to the rearmost part of the DTC edge.

Rotation of the DTC cap due to the applied torque is associated with a deformation of the gonad bulk region. We account for the intrinsic resistance of the gonad to deform by assigning a bending rigidity, B, to the midline axis of the gonad bulk, such that the bending energy of the gonad shape is given by

$$F_{bend} = \frac{B}{2}\int_0^L c(l)^2\, dl$$

where L is the length of the gonad and c indicates the curvature of the midline axis at each point.

Simulating DTC turning and gonad shape

Based on experimental estimates, we take the proliferation rate as constant. As the gonad elongates, at each time step we update the states of the cell-matrix adhesions and determine the optimal shape of the gonad bulk that minimizes the bending energy of the representative midline, F_{bend}. We account for the lateral-dorsal confinement of the gonad within the animal by imposing two parallel reflective boundaries, parallel to the original gonad orientation.

Starting from an initially straight gonad of length L=50 μm, we simulate the gonad elongation over a total length of $\Delta L = 100$ μm. We characterize the final morphology based on DTC position and orientation. The longitudinal position of the DTC relative to the rear, Δy, is defined such that positive values indicate DTC that are forward of the fixed rear position, while negative values indicate DTCs that have progressed further beyond that point. The DTC orientation angle, θ, is defined such that $\theta = \pm 180^\circ$ corresponds to the opposite orientation towards the rear. Negative θ values designate DTCs oriented in the dorsal direction, while positive values indicate the basal direction. Simulations for which the gonad develops the characteristic U-shape (DTC has moved past the fixed gonad end and is pointing towards the rear) as successful.

We characterize the effects of asymmetrical adhesion distribution along the DTC front by varying the magnitude of the adhesion strength, k_0, and the time fraction at which asymmetrical adhesions are engaged during the elongation phase, f_{as}. For convenience, we define the nondimensional adhesion strength as $\tilde{k_0} = k_0 \Delta_c^3/B$. Simulation results of Δy and θ values for were calculated for 254 representative points in the phase space and interpolated over the parameter ranges. Finally, we plot the phase space of the system by showing the gonad's ability to successfully complete a turn as a function of f_{as} and $\tilde{k_0}$.

Calculations and graphical output of the simulation were implemented using custom scripts for the Surface Evolver numerical optimization software (Brakke, 1992). The custom computer code is available at https://zenodo.org/record/6778907#.YrxOKi0RoWo.

QUANTIFICATION AND STATISTICAL ANALYSIS

GraphPad Prism 9 software was used to carry out all the statistical analysis. We used Student's t-test or Mann-Whitney test to determine p-value significance while comparing two samples. All the results in the graph are depicted as mean ± S.E.M. Each experiment was performed independently at least three or four times (N) and the exact number of gonads (n) analyzed are mentioned in the respective figure legends.